

Developing a Vector Light Sensor

by

Dong Hao Zhuo

B.A.Sc., Simon Fraser University, 2016

Thesis Submitted in Partial Fulfillment of the
Requirements for the Degree of
Master of Applied Sciences

in the
School of Mechatronic Systems Engineering
Faculty of Applied Sciences

© Dong Hao Zhuo 2019
SIMON FRASER UNIVERSITY
Spring 2019

Copyright in this work rests with the author. Please ensure that any reproduction or re-use is done in accordance with the relevant national copyright legislation.

Approval

Name: Dong Hao Zhuo

Degree: Master of Applied Science

Title: Developing a Vector Light Sensor

Examining Committee: **Chair:** Jason Wang
Assistant Professor

Behraad Bahreyni
Senior Supervisor
Associate Professor

Gary Leach
Supervisor
Associate professor

Ash M. Parameswaran
Internal Examiner
Professor
School of Engineering Science

Date Defended/Approved: Jan 10, 2019

Abstract

Over the past few decades, numerous sensors have been invented for the measurement of light intensity. In most cases, a setup external to the sensor is required to detect the direction of an incoming beam of light. In this work, the design, fabrication, and characterization of a novel light sensor is described. The three-dimensional structure of the sensor allows it to detect both the intensity as well as the direction of the incident light beam, hence becoming a vector light sensor (VLS). The sensor structure is based on creating photodiodes on sidewalls of miniaturized raised or inverted pyramids etched in silicon. Each photodiode was formed by selective doping of the material on each facet of the pyramid, forming a photodiode with the P-type substrate. A set of signal processing algorithms was developed to estimate the direction and the distance of a light source from the sensors. The light sensing devices with both raised and inverted pyramid structures were then fabricated in a cleanroom based on silicon microfabrication technologies. Throughout the process, the lithography step for the textured surface needed to be optimized. An interface circuit was designed and used to amplify and process the signals from the devices. The device operation was verified experimentally to estimate the direction of a light beam. The small size and low power consumption of the individual sensors make them suitable for applications where simple distance and direction estimation is required. The sensors can be arrayed to provide light-field information in the plane of sensor.

Keywords: Vector Light Sensor; PN-junction; angular light detection; nanofabrication

Dedication

World Peace

Acknowledgments

First of all, I would love to sincerely appreciate all the help and inspiration from my professor Dr. Behraad Bahreyni. He is a knowledgeable person who is always being patient to me and help me to solve the technical issues. He also provided me with a lot of opportunities to learn new knowledge in this field.

I also feel grateful with the help from all my lab partners when I had doubts and issues with my research. Abbin P. Joy is my good friend, and he always gives me great help when I was struggling with something in the study. Ashish Rai gave me a lot of help with the testing for VLS. Fan Xia is very knowledgeable, and she provided me with some theoretical knowledge which I never learned. Siamack Vosoogh-Grayli patiently taught and trained me with the equipment in the cleanroom.

Last but not least, I feel thankful to the members of my family. They always gave me mental support when I feel stressful or doubtful.

Table of Contents

Approval	ii
Abstract	iii
Dedication	iv
Acknowledgments	v
Table of Contents	vi
List of Tables	viii
List of Figures	ix
List of Acronyms	xi
List of Symbols	xii
Chapter 1. Introduction	1
1.1. Background	1
1.2. Motivation and objective	2
1.3. Thesis outline	4
Chapter 2. Literature review	6
2.1. Semiconductor light sensors	6
2.1.1. Photoresistors	6
2.1.2. Photodiodes	7
2.1.3. Charge-coupled Devices	9
2.2. Current approaches for detection of light direction	10
2.2.1. Systems using a slot for light passage	10
2.2.2. Systems based on light waveguides	11
2.2.3. Systems based on sensors mounted on 3D structures	13
2.2.4. Prototype with a pyramid base	13
Chapter 3. Operating Principle	16
3.1. Detecting the 2D direction of a light source	17
3.1.1. Operating principles	17
3.2. Detecting the 3D direction of a light source	19
3.2.1. Estimating the angle φ	20
3.2.2. Estimating the angle θ	24
3.3. Detecting the position of a light source in 3D space	26
3.3.1. Detecting vertical distance from the sensor of a light source	26
3.3.2. Detecting the position in 3D space	27
3.4. Inverted pyramid and its mathematical model	28
Chapter 4. Fabrication Process	30
4.1. Microfabrication steps	30
4.2. Fabrication steps	31
4.2.1. P-type silicon substrate selection	31
4.2.2. Thermal oxidation	33
4.2.3. Lithography for mask #1	33

4.2.4.	Etching the oxide layer	34
4.2.5.	Etching the substrate	34
4.2.6.	Oxidation for Mask #2	36
4.2.7.	3D lithography for Mask #2	36
4.2.8.	Pre-implant Oxidation.....	38
4.2.9.	N-type dopant ion implantation	38
4.2.10.	Oxidation/ Annealing	40
4.2.11.	3D lithography for Mask #3.....	40
4.2.12.	Metallization.....	43
4.2.13.	Packaging.....	44
4.3.	Corner compensation for raised pyramids	45
4.4.	Optimization of 3D lithography	48
4.5.	Ion implantation vs. diffusion	50
4.6.	SEM images for devices	53
Chapter 5. Results and Device Characterization		56
5.1.	Diode characterization	56
5.1.1.	Forward bias region	56
5.1.2.	Reverse bias region	57
5.1.3.	Sensitivity to light	58
5.2.	Test setup	60
5.2.1.	Data processing	60
5.2.2.	Testing interface.....	61
5.3.	Device functionality testing.....	62
	Estimating the angle β	64
	Estimating the angle θ	67
	Estimating the angle φ	68
Chapter 6. Conclusions and future work		69
References.....		71
Appendix A. Fabrication details		76
	Details of silicon anisotropic etching process	76
	Details of the fabrication process	77
Appendix B. Feasible parameters for wire bonding		82

List of Tables

Table 3-1 Reference angle calculation	22
Table 3-2 Algorithm for finding ϕ	22
Table 4-1 Specifications of a silicon wafer provided by the manufacturer	32
Table 5-1 Parameters for the beams for 2D angle estimation.....	63

List of Figures

Figure 1-1 Cross-sectional and top views of the Raised (left) and Inverted Pyramid vector light sensors	3
Figure 2-1 A commercial photoresistor [24].....	6
Figure 2-2 Illustration of photo current in a PN-junction	8
Figure 2-3 Structure and working principle of CCD.....	9
Figure 2-4 Top view (left) and cross-section (right) of slotted light sensor	10
Figure 2-5 Top view of light sensor with slot for light passage	11
Figure 2-6 PIR motion sensor	12
Figure 2-7 Structure of a sun sensor	13
Figure 2-8 3D geometry of vector light sensor.....	14
Figure 2-9 Working mechanism of VLS system [33].....	15
Figure 3-1 The 3D structure of VLS	16
Figure 3-2 2D light direction estimation.....	17
Figure 3-3 Detection of the direction of light in 3D space in spherical coordinates	19
Figure 3-4 Angles β_{ns} and β_{we} in spherical coordinates	20
Figure 3-5 Quadrants in XY-plane	21
Figure 3-6 Matlab simulation of φ estimation.....	23
Figure 3-7 Estimating θ by using Pythagorean theorem.....	24
Figure 3-8 Matlab simulation of θ estimation	25
Figure 3-9 Method for finding vertical distance of a light source	26
Figure 3-10 Direction estimation in 2D with inverted pyramid	28
Figure 4-1 Main steps for the device fabrication. Note that passivation steps are skipped for brevity.	30
Figure 4-2 3D Structure Device Simulation	31
Figure 4-3 Fabrication process steps: Thermal oxidation and photoresist deposition	32
Figure 4-4 Fabrication process steps: Thermal oxidation and photoresist deposition	34
Figure 4-5 Fabrication process steps: Silicon etching, oxide etching and oxidation	35
Figure 4-6 Spray coater	36
Figure 4-7 Fabrication process: 3D lithography for Mask #2.....	37
Figure 4-8 Fabrication process: Ion implantation.....	38
Figure 4-9 Simulation of doping profile on the flat silicon surface (top) and on the side walls (bottom).....	39
Figure 4-10 Microscope screenshot of inverted pyramid after Mask #3 3D lithography	41

Figure 4-11 Microscope screenshot of raised pyramid after Mask #3 3D lithography	41
Figure 4-12 Fabrication process: 3D lithography for Mask #3.....	42
Figure 4-13 Fabrication process: Metallization	43
Figure 4-14 Picture of the wafer after lift-off.....	44
Figure 4-15 Wire bonded package.....	45
Figure 4-16 Square-shaped design for compensating structures.....	46
Figure 4-17 Raised structure designed for 60um with 20um height	47
Figure 4-18 Raised structure designed for 60um with 60um height	48
Figure 4-19 Post development silicon wafer surface with bubbles	49
Figure 4-20 Voltage sweep between two N-regions of neighbor diodes	50
Figure 4-21 IV plot for voltage sweep between two N-regions of neighbor diodes	51
Figure 4-22 IV plot for voltage sweep between two N-regions of neighbor diodes with a diode from the second fabrication run.....	52
Figure 4-23 SEM image for raised pyramid	53
Figure 4-24 SEM image for raised pyramid at the corner.....	54
Figure 4-25 SEM image for inverted pyramid	55
Figure 5-1 IV curve of a diode on the fabricated device with voltage sweeping from 0V to 1V	57
Figure 5-2 IV curve of a diode on the fabricated device with voltage sweeping from -11V to 0V	58
Figure 5-3 Irradiance vs. reverse diode current with different reverse voltages for a diode from VLS	59
Figure 5-4 Device testing interface.....	61
Figure 5-5 Device testing environment and light source	62
Figure 5-6 Light beams for testing the functionality of the VLS.....	63
Figure 5-7 Comparison between estimated angles and actual angles for β_{NS} with one device and 10 repeated measurements	64
Figure 5-8 Comparison between estimated angles and actual angles for β_{WE} with one device and 10 repeated measurements	65
Figure 5-10 Comparison between estimated angles and actual angles for β with six pairs of optical detectors on pyramids	66
Figure 5-9 Comparison SEM image of a raised pyramid.....	66
Figure 5-11 Comparison between estimated angles and actual angles for θ.....	67
Figure 5-12 Comparison between estimated angles and actual angles for ϕ.....	68

List of Acronyms

BJT	Bipolar Junction Transistor
BOE	Buffered oxide etch
CCD	Charged-coupled device
DIP	Dual-In-Line Package
HMDS	Hexamethyldisilazane
IC	Integrated Circuit
IPA	Isopropyl Alcohol
KOH	Potassium Hydroxide
PIR	Pyroelectric Infrared Sensor
PR	Photoresist
SEM	Scanning Electron Microscope
SIMS	Secondary ion mass spectrometry
SMU	Source measure unit
VLS	Vector Light Sensor

List of Symbols

I_d	Diode current
η	Quantum efficiency
I_p	Photocurrent
e	Electron charge
R_{lr}	Ratio of left over right signals
α	Angle between the sensor and horizon
β	Angle of inclination to the light source
φ	Azimuthal angle
θ	Polar angle
r	Radius

Chapter 1. Introduction

1.1. Background

Numerous light sensing technologies have been developed over the past several decades. There are numbers of applications from different designs with light sensitive materials. Estimation of the direction and the distance between a light source and objects is of great importance in many fields. Examples include driver assistance systems, gesture-based interfaces, collision/injury avoidance systems, security, manufacturing, industrial automation, etc. In a more specific case, industrial robots [1], [2] are gradually replacing human labor in most manufacturing situations. An industrial robot is a re-programmable, automatically controlled and multipurpose manipulator that can maneuver in three or more axes. Typical applications of robots include welding, painting, assembly, pick and place, product inspection and testing; all accomplished with high endurance, speed, and precision. However, typical industrial robots are programmed and operate automatically. It is shown that the productivity in factories improves significantly if human workers can collaborate with robots along the production line. The field of robotics may be defined as the study, design, and use of robot systems for manufacturing. In collaborative environment, however, they might produce accident and injury to a human if workers are nearby. The initial driver for this research was the development of small-profile proximity sensors to improve the safety of humans in such collaborative work environments.

Short distance light detection is currently performed through different techniques. Video cameras in combination with video processing software are used in many applications to detect, locate, and even identify humans [3]–[6]. An alternative technique for the detection of humans is using ultrasonic transmitters and receivers [7] since different environmental phenomena produce a significant amount of ultrasound noise which requires operation at relatively high frequencies.

If cameras are picked as an option, their performance will be limited due to the inevitable blind-spots especially considering various approach angles between workers and robots for longer distance (i.e., >5m) [8], [9]. Furthermore, the limited field of view of video cameras restricts their application in close-range interactions (i.e., <2m). On the

other hand, video cameras are made of optical and electronic components, making them fragile and bulky and limiting their applications.

For light sensing at extended ranges with less power consumption, photoresistors and photodiodes [8],[9] are suitable components in designs for current commercial products sensors integrated with photodiodes and photoresistors were invented and broadly used in the industrial field. A few of the devices for detecting the direction of the light were developed with photodiodes in arrays sitting inside the structured enclosures or substrates. For example, sun sensor being used by researchers working in the space is created by photodiodes in arrays inside a cubic structure. All the information from the photodiodes has to be captured to estimate the direction (see section 2.2). In this case, processors have to access tens of data in real time, and they are power consuming.

1.2. Motivation and objective

The motivation behind this research is to develop a light-based proximity sensor for industrial robotic applications. Estimation of distance in this case relies on triangulation of the source using two vector light sensors that independently provide angles of inclination to a source. The devices should be able to be used in applications where it is necessary to estimate the distance between objects within a range of about 10cm to 5m. The distance estimation relies on the 3D geometry and placement of several light sensing elements on a pyramidal based. A macro-model of the device was fabricated and successfully tested within our group. The aim of this research is to produce an integrated sensing device with photodiodes at micro-scales to pave the way for further integration of such devices with each other or with active electronics.

Using photodiodes as the main elements of the sensor fits both low power consuming and detecting range requirements. Currently, several devices for detecting the direction of light were fabricated in micro-scale but with bulky packages, for example, pyroelectric infrared motion sensor [12]. Also, the devices were integrated with tens of elements which are power consuming. As a result, the objective of this research was to design a silicon-based device with limited numbers of photodiodes that is able to detect the direction and the position of a light source.

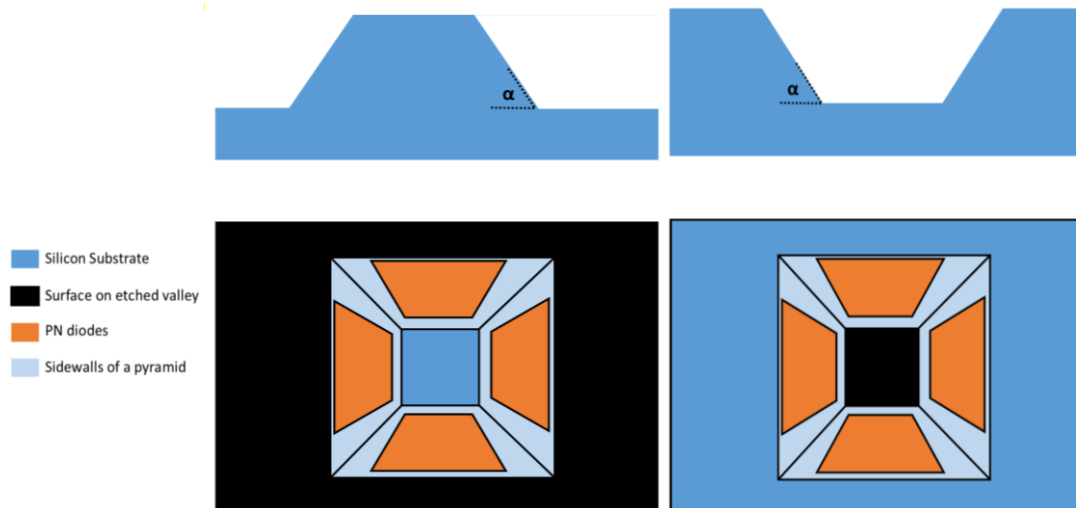


Figure 1-1 Cross-sectional and top views of the Raised (left) and Inverted Pyramid vector light sensors

The device base is a pyramid that is either raised or inverted with respect to the substrate with four light-sensitive areas on the pyramid sidewalls facing four different directions. A schematic of the vector light sensor (VLS) is shown in figure 1-1, where the orange areas indicate the locations sensitive to visible light sources. The four trapezoidal sensing areas will measure the same signal amplitude if the incident light source is normal to the top surface of the VLS. However, if the same light source inclines, the trapezoidal sensors will respond to different amounts of output amplitudes depending on the angle of the incoming incident light source to each sensor. As a result, it is possible to estimate the direction of the incoming visible light by comparing the signals from the four trapezoidal sensing areas. Moreover, to provide also a distance estimation of the light source, it is possible to use two VLS and employ a simple triangulation technique.

The calculating method of estimation was developed with trigonometry techniques. In the beginning, the algorithm was proven by a prototype with four commercial photodiodes sitting on sidewalls of a 3D-printed raised pyramid structure.

The next step was to implement and microfabricate the designed structure. The motivations for miniaturization of the device are:

- *Arrayed sensors:* With one VLS device, the 3D information of one light source could be captured. If more than one VLS devices were arranged in array, more information could be extracted from the surroundings. It is necessary to downsize

the device from macro- to micro-scales if a light sensing system has hundreds of VLS devices.

- *Integration with electronics:* After the light sensing system with VLS devices was implemented and fabricated into a silicon base chip, it will be wire-bonded to a package with desire number of pins and size. Packages with micro-scale devices are easier to integrate with other electronics components.
- *Large scale manufacturing:* The VLS device could be used numerous applications in various industries. In such a case, large scale manufacturing will be one of the major considerations. Miniaturizing the device and manufacturing the devices with MEMS technologies make the process low in cost.

The pyramid structure was created by etching silicon surface with potassium hydroxide (KOH) [13]–[15]. The four trapezoidal sensing areas were formed by doping N-type material on P-type silicon substrate.

The small size and low power consumption of the individual sensors make them suitable for applications where simple distance and direction estimations required. This lets such sensors to be integrated into many systems, including mobile computing devices. The arrayed sensors can provide information about the surroundings in 3D and can have many applications as replacements for current 3D imaging systems while providing opportunities for new application. The significant advantage of this technology over the existing solutions is its full field of view and the possibility of operation without optical lenses.

1.3. Thesis outline

The thesis is divided into six chapters as follows:

Chapter 1 provides a general introduction of background knowledge and motivation of this thesis work.

Chapter 2 discusses different light-sensitive materials and comparing different methods for light source detection in history.

Chapter 3 introduces the mathematical model of the light sensing system.

Chapter 4 explains a step-by-step description of the micro-fabrication process which is developed by the author to fabricate the micro-device. Detailed process steps are included in Appendix A of this thesis.

Chapter 5 provides an overview of the experimental test setup, signal processing for the fabricated devices, and the discussion of the testing results.

Chapter 6 concludes the thesis by revisiting the challenges of the estimation by the fabricated device with specific light sources and by summarizing the major achievements of the research. Also, it represents perspectives of future works.

Chapter 2. Literature review

The objective of the project is to detect and track a light source in real time using a sensing system that relies on a number of VLS to detect both the direction and intensity of the light from the source. There are many ways to fulfill this application such as a system based on orthogonal sensors, slotted structures for light passage, light waveguides and sensors mounted on a 3D geometry.

2.1. Semiconductor light sensors

Photodiode and phototransistors have been used since the 1800s for light detection [16]. With the rapid development of micro/nano-technologies over the past few decades, the devices have been improved and broadly used in the industries. Numerous semiconductor sensors are nowadays used for many different applications, ranging from ambient light sensing to optical communications.

2.1.1. Photoresistors

A photoresistor is a light-dependent or light-controlled variable resistor [8]. The resistance of a photoresistor varies with the intensity of light. The resistance increases with decreasing incident light intensity. Since light dependent photoresistors have lower sensitivity than photodiodes and phototransistors, photoresistors are broadly used for the applications that do not require high accuracies such as solar street light, night lamp and

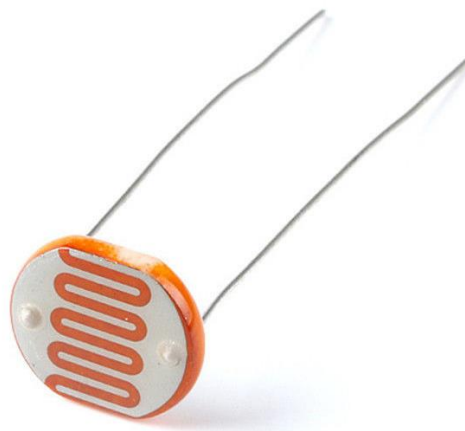


Figure 2-1 A commercial photoresistor [24]

outdoor clocks [17],[18]. There are two types of materials for photoresistors which are intrinsic and extrinsic [19]. Intrinsic photoresistors use undoped materials such as silicon or germanium [20]. Moreover, since light dependent resistors are generally designed for detecting lights with long wavelengths [21],[22], they are also used as IR sensors. Figure 2-1 shows a picture of a commonly used photoresistor.

An easy lamp control circuit without microcontroller could be made with a light bulb and a photoresistor in series powered by a constant voltage. The light intensity of the light bulb will then vary continuously with the changes of ambient light hitting on the surface of the photoresistor [23],[24].

2.1.2. Photodiodes

A photodiode is a semiconductor device that converts the energy of incident light into an electrical current [25]. The current is generated when photons are absorbed in the photodiode. Any PN junction is potentially a photodiode. The material we are using for fabricating the device is silicon which is a typical diode material, and the PN junction could detect a light source with wavelengths from 190nm to 1.1um [9]. Figure 2-2 shows the illustration of photo current in a pn-junction. The device in the figure is a flat PN junction with the P-type silicon substrate and the N-type doped region on top. Once a small voltage is supplied on the diode as shown, the diode will be in the reverse-bias region. Initially, the positive terminal attracts electrons from the N region and vice versa. Free space between the electrons and holes is created which is as known as the depletion region. Meanwhile, an electric field is formed in the depletion region from the N-side of the junction to the P-side. When the device is in a dark environment, there will be nearly no current going through the close-loop circuit except for some leakage current of the diode. However, when an external light energy is applied to the depletion region, the valence electrons gain energy. Once the valence electrons gain enough energy and break bonds with the parent atoms, they will become free electrons and move freely in the depletion region. At the same time, free electrons will accelerate and travel towards N region due to the internal electric field. High valence electron energy will cause high kinetic energy of the photo generated carriers. Therefore, the electrons will break through the depletion region and enter the N region. Once the free electrons enter the N region, they will be attracted towards the positive terminal of the power supply. Similarly, free holes will similarly travel towards the negative terminal. Finally, reverse-bias current will be

generated due to the external photon energy applied to the surface of the device. The higher is the light intensity incident on the surface, the higher will be the generated photocurrent.

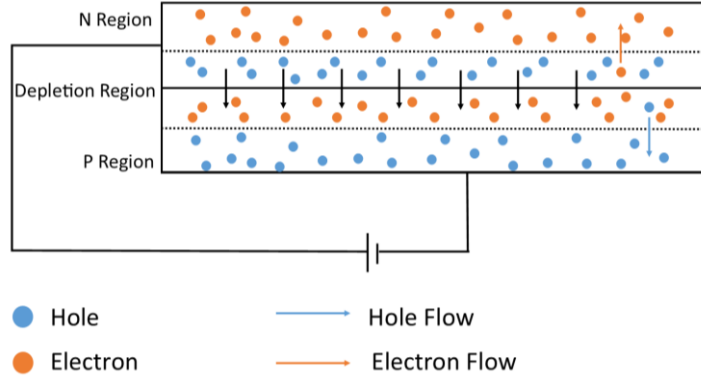


Figure 2-2 Illustration of photo current in a PN-junction

A standard diode equation is as followed [26]:

$$I_d = I_{s0} \left(e^{\frac{V_d}{nV_T}} - 1 \right) + I_p \quad (1)$$

where I_d is the total current of the diode, I_{s0} is the saturation current of the diode, n is the ideality factor (typically between 1 and 2), and I_p is the photocurrent which is varying with the change of light intensity. The saturation current, I_{s0} , is a function of carrier concentration, N-type and P-type doping concentrations and the size of the device. Under reverse-bias conditions, the current through the diode will be essentially constant at $I_{d0} \approx -I_{s0}$ regardless of the voltage drop across the diode, (up to about the breakdown region). Therefore, the only component that can vary is the diode current with the number of incident photons, I_p . There is an essential parameter of a photodiode, which is called quantum efficiency [26]. The quantum efficiency of a photodiode is its ability to convert photon energy into electrical energy, often percentage. The expression is shown below [9]:

$$\eta = \frac{r_e}{r_p} = \frac{\# \text{ of electrons collected as } I_p/\text{sec}}{\# \text{ of incident photons/sec or photon flux}} \times 100 \quad (2)$$

Simply put, quantum efficiency is the percentage that a photodiode can transfer photon energy to electrical energy. Moreover, this parameter depends on the diode structure, its thickness, doping, geometry, and so on. The total electric current converted from photon energy will be:

$$I_p = e r_e = e \eta r_p \quad (3)$$

where e is the charge of an electron. As a result, the photocurrent through a diode is directly proportional to the intensity of incident light.

2.1.3. Charge-coupled Devices

A charged-coupled device (CCD) [27] is a device stores and displays data of an image by converting the optical information into electrical charge. The difference between CCD and photodiode is that CCD is converting photon energy into electronic charge and CCD can store the information as digital value. There are different kinds of CCDs for different application, but they can all be defined merely as a charge transfer device [28]. The simple working principle of the device is demonstrated in Figure 2-3 which shows one of the CMOS devices formed in arrays for the CCD. With different combination of the voltage applied to the gate terminal, different transfers of change packets were created accordingly. The sequence of voltages is sampled, digitized and then stored in memory for the application of digital camera nowadays.

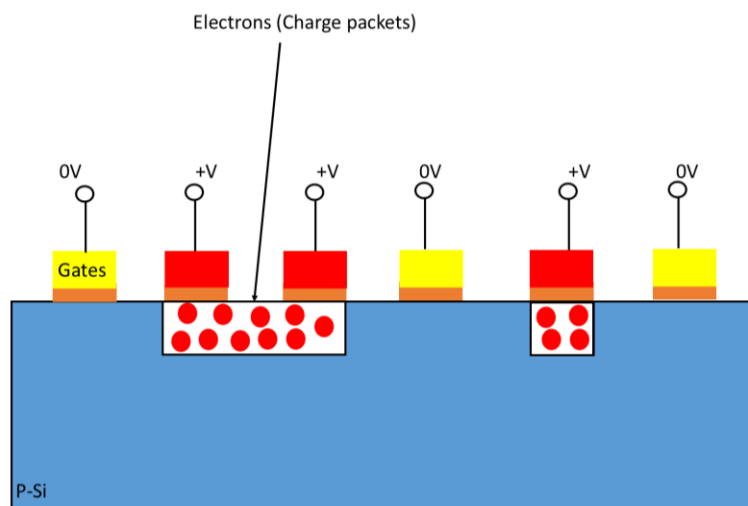


Figure 2-3 Structure and working principle of CCD

2.2. Current approaches for detection of light direction

2.2.1. Systems using a slot for light passage

Sensor systems based on the slot for light passage were invented in the past with light sensors on the same plane for detecting the direction of a light source. Figure 2-4 shows the cross-section for one of the examples for such a system by Zivkovic et al. in 2014 [29]. The integrated sensor chip package was fabricated with a four by four matrix of photodiodes. The light blocking material has a square-shaped opening to allow light to pass through. With light sources from different directions, different output combinations would result from the photodiodes on the substrate. An integrated circuit (IC) was also on the substrate with the photodiodes in the body of the device. Finally, the data was exported to an external microcontroller and processed to calculate the direction of the light beam. Based on the combination of the array, the size of the opening and the vertical distance between the substrate and the opening, the direction of the light from a given source could be estimated.

For distance estimation from the light source to sensor, a modification was done as shown in Figure 2-5. An extra set of photodiodes packaged array was added. Therefore, two more variables were known for the estimation: another direction of the light source regarding to the additional sensor, and the distance between the centers of the two openings. With the three values, the distance between the light source and the sensor could be calculated by using trigonometry [30].

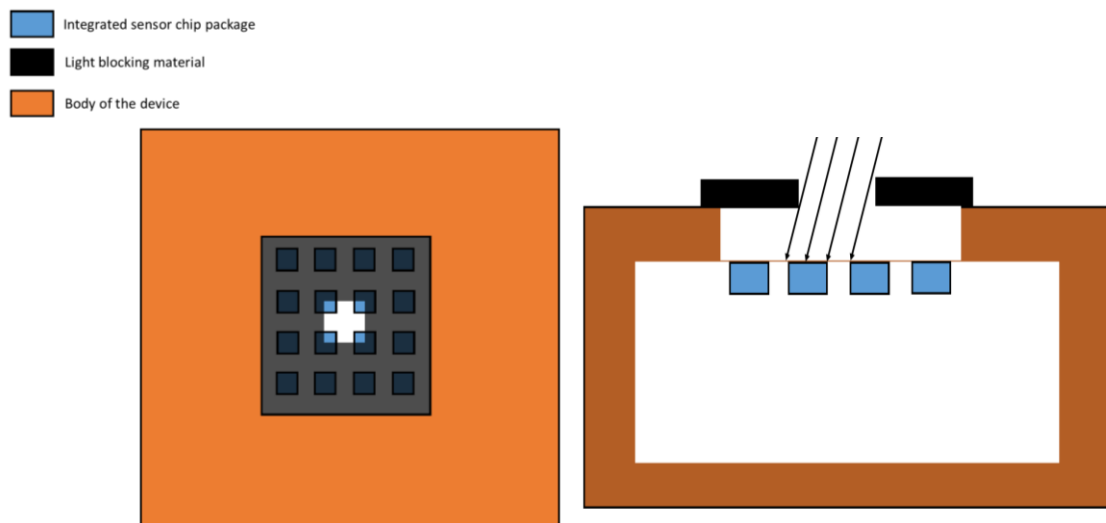


Figure 2-4 Top view (left) and cross-section (right) of slotted light sensor

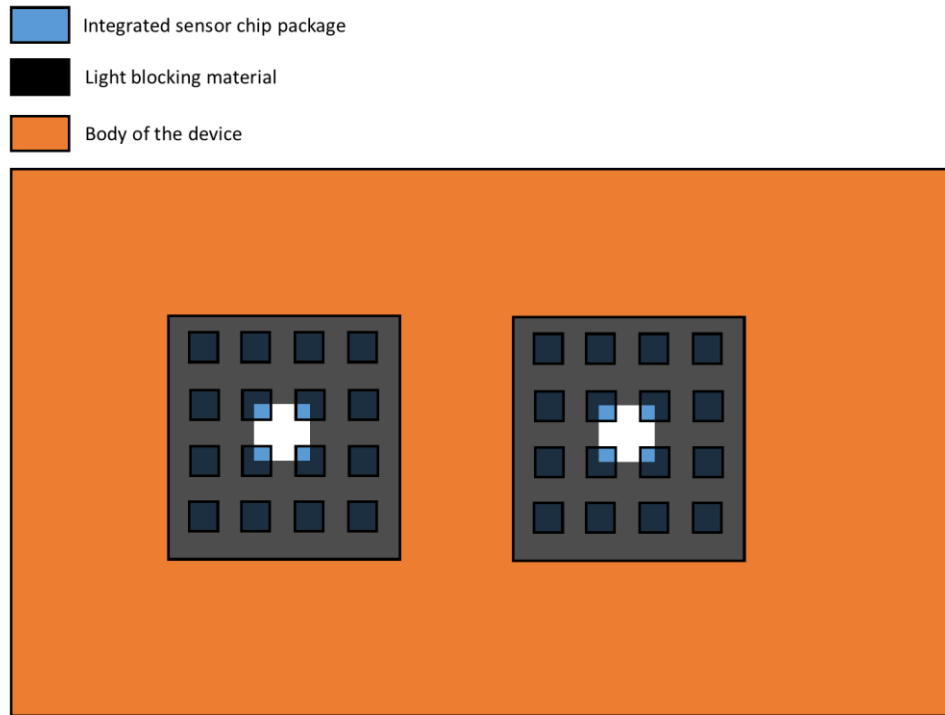


Figure 2-5 Top view of light sensor with slot for light passage

2.2.2. Systems based on light waveguides

One of the most popular methods to track and detect a light source is based on spherical sensors with multiple detectors in front of waveguides.

An optical waveguide is a structure that transport energy at wavelengths of the electromagnetic spectrum [31]. Waveguides been used with different materials for different applications:

Lens waveguides: Light beams can be formed and propagated by a system created by lenses and mirrors [32].

Metallic waveguides: Usually being used as a tool for extreme confinement of TeraHertz surface waves [33].

Dielectric waveguides: Currently, the most popular method to make waveguides because of the very low absorption and scattering losses during the transportation of light [34]. The waveguides exist in two different forms: Planar dielectric film waveguides (1D-guiding) and cylindrical fiber waveguides (2D-guiding).



Figure 2-6 PIR motion sensor

A typical application of dielectric waveguides is Pyroelectric Infrared sensor (PIR). Most of the PIR sensors are covered by a shield with multiple waveguides on semi-spherical 3D models. Figure 2-6 shows the picture of a commercial PIR motion sensor.

The waveguides are distributed in arrays to make the pyroelectric sensor inside the shield be able to detect human-radiated IR waves from different space segments within 5 to 10 meters. Many of the PIR sensors are bundled with light bulbs and microcontrollers so that they can be used as motion sensing light switches for night time use. However, the sensors mentioned above are with low precision and accuracy base on the materials of the sensors and the requirements for the applications.

2.2.3. Systems based on sensors mounted on 3D structures

Another method to detect the direction of a light beam is to use light sensors that collect light from different directions and then compute the direction based on the relative amounts of light received by each sensor. Sun sensors that are used for space travel are well-known examples of such devices [35]–[37]. Figure 2-7 indicates the structure of the light sensing system. The application of the sun sensor is to only detect the direction of the sun as the dominant light source. It is an extension of the sensor mentioned in section 2.2.1. Instead of recognizing the light source in the semi-spherical coordinate, the sensor can detect the direction and the location of the sun. As shown in Figure 2-7, the sun sensor has a cubic shape. There are light sensing materials mounted on each sidewall of the cube. Similarly, the information of the sun could be detected with the combination of the outputs from sensors on sidewalls facing different directions.

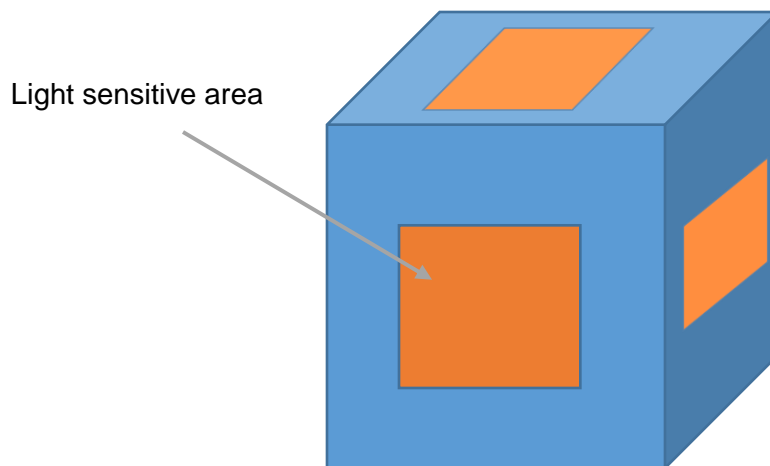


Figure 2-7 Structure of a sun sensor

2.2.4. Prototype with a pyramid base

A system that mount sensors on a 3D geometry was developed by graduate students from Intelligent Sensing Laboratory in 2016 as a macro-scale model for the current micro-fabricated sensor [38]. A 3D geometry model was designed by Solidworks and created by the 3D printing machine. Figure 2-6 shows the developed 3D raised pyramid structure for the light sensing device. The width of the pyramid structure was 1cm by 1cm, and the height was 0.5cm.

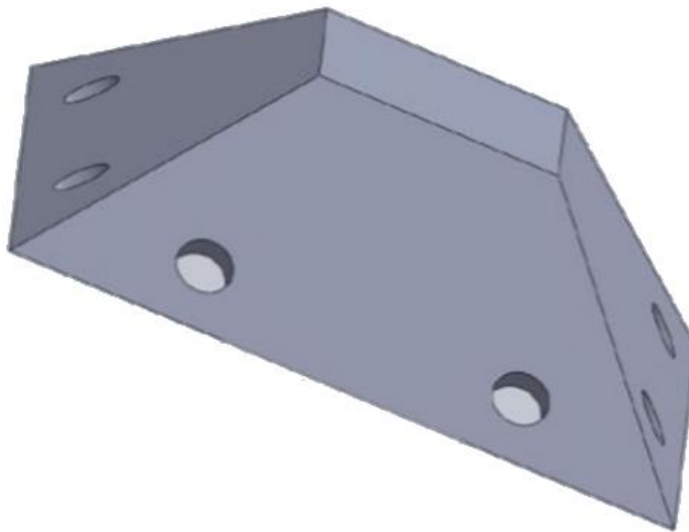


Figure 2-8 3D geometry of vector light sensor

The holes on the sidewalls of the pyramid were for the terminals of photodiodes going through the construction and connected on either a breadboard or a printed circuit board. Four manufactured photodiodes were mounted on sidewalls of the pyramid by carbon tapes. The angles between the sidewalls and the horizon were 45° instead of the fabricated device introduced in Chapter 3 to have a broader range of detection.

The primary working mechanism of a photodiode is that the reverse bias current varies with the changing of the light intensity impeding on the surface of itself [39]. By comparing a pair of photodiodes facing opposite directions and on the same pyramid, the 2D directional angle to the source could be estimated.

Modification of the device modeling and the equations for calculation of 2D vertical distance estimations, 3D direction estimations and 3D positions estimates are all based on the results calculated from equations developed with this device. Details of the algorithm are introduced in chapter 3.

Figure 2-9. A shows the schematic of the system, and Figure 2-9.B is a screenshot of the assembled photodiode-based vector light sensor [40]. Eight photodiodes are connected in parallel to a power source. Each photodiode is connected to a set of components including op-amp and an NPN BJT as shown in Block A. Photodiode D1 is placed on a flat surface while four photodiodes are placed on pyramids 1 and 2. Each

photodiode is connected to a set of components similar to Block A components B shows an image of photodiodes on a 3D printed pyramid.

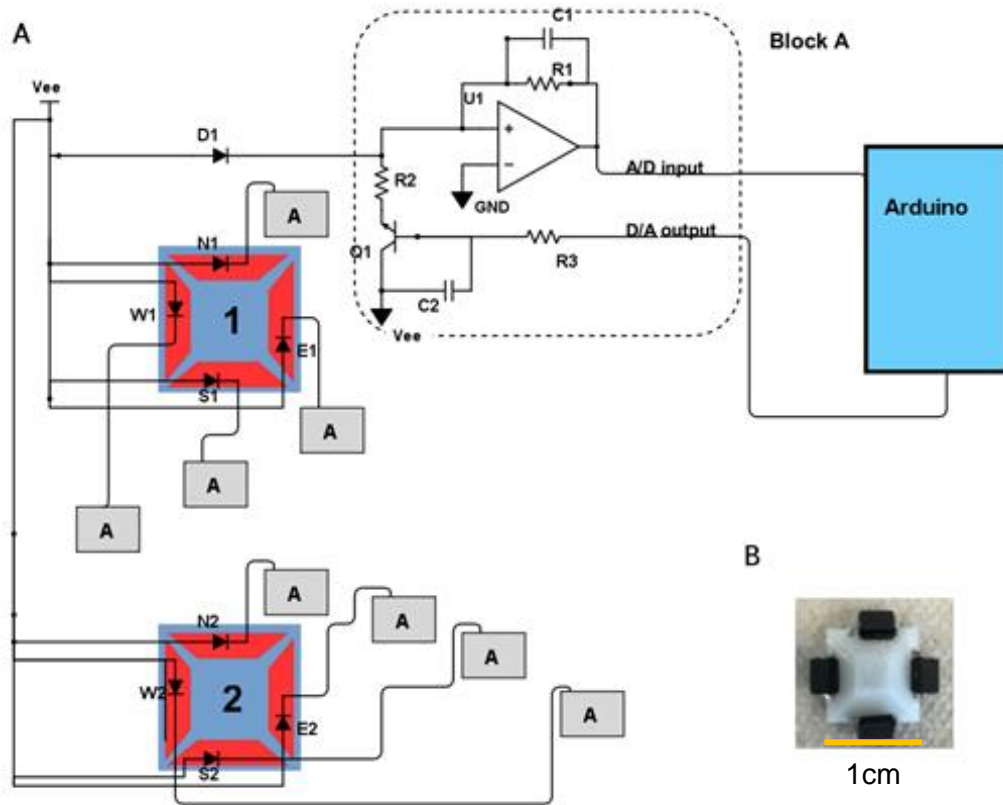


Figure 2-9 Working mechanism of VLS system [33]

From the schematic diagram, D1 is a reference photodiode for detecting the background light. The current generated by D1 flowed through R1 and transferred into voltage. The output voltage was then read by the analog-to-digital converter of an Arduino board. Meanwhile, the digital-to-analog converter of the board produced a voltage on one side of R3 in real time. D/A voltage kept on increasing until A/D input was zero. This method canceled out the current generated due to the background light. After the cancellation of the background light, all the outputs from photodiodes on the pyramid were collected by Arduino A/D and used for the angular estimation algorithm in real time.

Chapter 3. Operating Principle

This chapter discusses the primary mechanisms to detect the direction and distance to a light source by using one or two pyramid structures and several PN diodes. The main approaches for the light sensing will be:

- 1) Detecting the 2D direction of a light source which is the angle between the incident light and the horizontal axis by comparing the output signals of the PN diodes facing two opposite directions from a single pyramid structure.
- 2) Detecting the 3D direction of a light source with the sensor by comparing all the four photodiodes sitting on each side of a single pyramid structure.
- 3) Detecting the actual coordinate of a light source in the 3D space by using two pyramids at a certain distance.

Figure 3-1 shows the 3D view and the top view of the pyramid structure for the designed light sensor. As we can see, each sensor is a three-dimensional structure having four light sensitive surfaces that face predetermined directions.

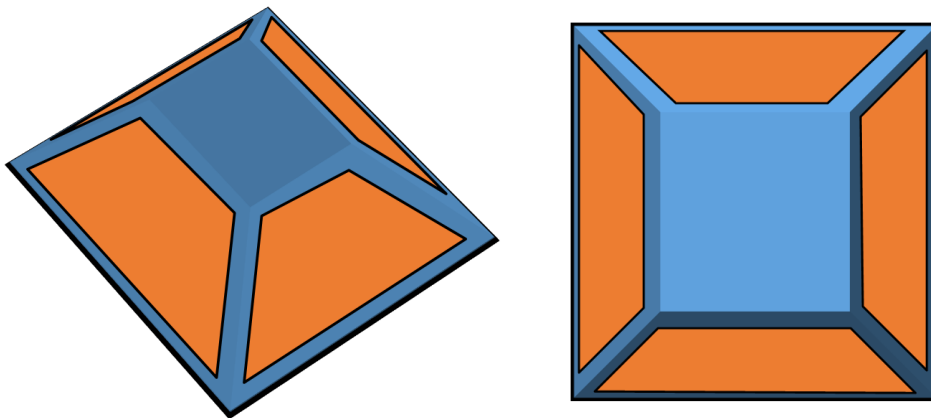


Figure 3-1 The 3D structure of VLS

3.1. Detecting the 2D direction of a light source

3.1.1. Operating principles

As discussed in section 2.1.2, the ratio of the photocurrents between diodes is the same as the ratio of the incident photon energy or the flux of light applied at the diodes. Furthermore, by comparing the output signals from the diodes, we could backtrack and calculate the estimated position of a light source. Figure 3-2 indicates the 2D model of the light sensor. α is the angle between a detector sitting on a sidewall of the pyramid and the horizontal axis. Throughout the project, the value of α will be 54.75° since the fabrication procedure for creating the pyramid structure will use potassium hydroxide silicon etching [41]. We assume the light rays are parallel and uniformly applied on the sensor. β represents the angle between the incident beam of light and the horizon.

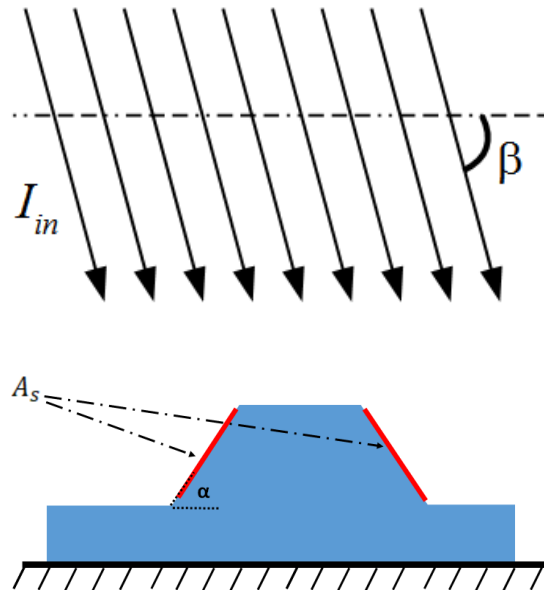


Figure 3-2 2D light direction estimation

Moreover, A_s represents the sensing area of each photodiode and I_{in} is the light intensity of the source which is assumed to be uniform over the sensor area. The powers of light on both photodiodes $P_{l,inc}$ and $P_{r,inc}$ can be represented by A_s , I_{in} , α and β :

$$\begin{cases} P_{l,inc} = A_s I_{in} \sin(\beta + \alpha) \\ P_{r,inc} = A_s I_{in} \sin(\beta - \alpha) \end{cases} \quad (4)$$

Taking a ratio between $P_{l,inc}$ and $P_{r,inc}$:

$$R_{lr} = \frac{\sin(\alpha+\beta)}{\sin(-\alpha+\beta)} \quad (5)$$

With this model, we call the diode current captured from the diode on the left side I_{left} and the other one I_{right} . Since the power of incident photons is proportional to the photocurrent, therefore:

$$R_{lr} = \frac{I_{left}}{I_{right}} = \frac{\sin(\alpha+\beta)}{\sin(-\alpha+\beta)} \quad (6)$$

The next approach is to solve the equation so that β can be an expression regarding α and right-left currents ratio.

$$R_{lr} = \frac{\sin(\alpha+\beta)}{\sin(-\alpha+\beta)} = \frac{\sin(\alpha+\beta)}{\sin(\alpha+\beta-2\alpha)} = \frac{\sin(\alpha+\beta)}{\sin(\alpha+\beta)\cos(2\alpha)-\sin(2\alpha)\cos(\alpha+\beta)} \quad (7)$$

Re-arrange the equation (7):

$$R_{lr} \sin(\alpha + \beta) \cos(2\alpha) - R_{lr} \sin(2\alpha) \cos(\alpha + \beta) = \sin(\alpha + \beta)$$

$$\sin(\alpha + \beta) (R_{lr} \cos(2\alpha) - 1) = R_{lr} \sin(2\alpha) \cos(\alpha + \beta)$$

Moving ratios to the same side:

$$\frac{\cos(\alpha+\beta)}{\sin(\alpha+\beta)} = \cot(\alpha + \beta) = \frac{R_{lr} \cos(2\alpha)-1}{R_{lr} \sin(2\alpha)} \quad (8)$$

Therefore, β could be expressed as:

$$\beta = \cot^{-1} \left(\frac{R_{lr} \cos(2\alpha)-1}{R_{lr} \sin(2\alpha)} \right) - \alpha$$

However, the domain of $\text{acot}(x)$ function is $x \neq 0$. Unfortunately, it is possible that the ratio of the diodes $R_{lr} = \frac{1}{\cos(2\alpha)}$ which will make the function undefined. Therefore, an alternate expression from equation (8) is derived:

$$\tan \left(\frac{\pi}{2} - (\alpha + \beta) \right) = \frac{R_{lr} \cos(2\alpha)-1}{R_{lr} \sin(2\alpha)}$$

Finally,

$$\beta = \frac{\pi}{2} - \alpha - \text{atan}\left(\frac{(R_{lr} \cos(2\alpha) - 1)}{R_{lr} \sin(2\alpha)}\right) \quad (9)$$

3.2. Detecting the 3D direction of a light source

To estimate and represent the direction of a light source in the 3D space, spherical coordinates could be applied. Figure 3-3 shows the spherical coordinates (r, θ, φ) as commonly used in physics: radial distance r , polar angle θ ($0^\circ < \theta < 180^\circ$) and azimuthal angle φ ($0^\circ < \varphi < 360^\circ$) [42]. The sensor is located at the origin of the coordinates, and the diode facing to the North of the pyramid is pointing the positive x-axis direction.

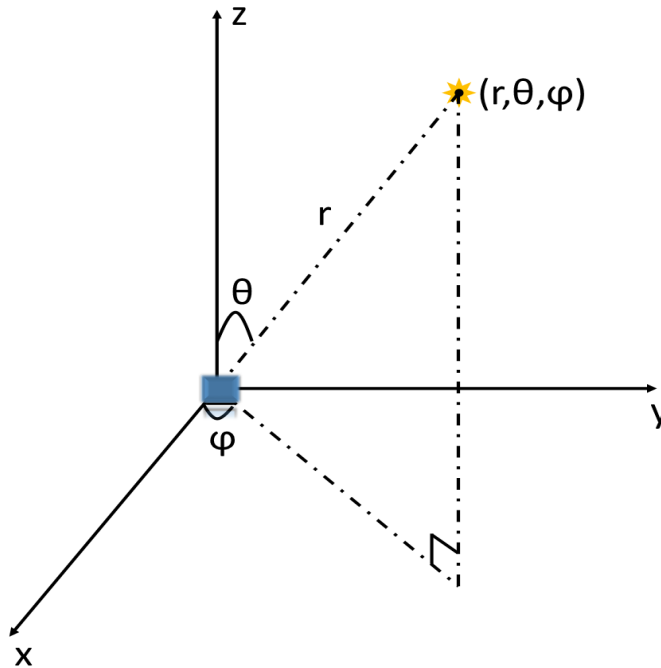


Figure 3-3 Detection of the direction of light in 3D space in spherical coordinates

Using the opposite pair of sensors on the pyramid, we can estimate the 2D angle β as introduced in the previous section. Therefore, with one pyramid, there will be two angles generated when detecting a light source which is from the one calculated with North-South diode pair, and the one with West-East. For convenience, we will name the two angles β_{ns} and β_{we} . By using the pair of information, we can estimate both θ and φ . The distance r could be calculated only if another pyramid is included with a certain

distance from the pyramid at the origin. The distance estimation will be introduced in the upcoming section.

3.2.1. Estimating the angle φ

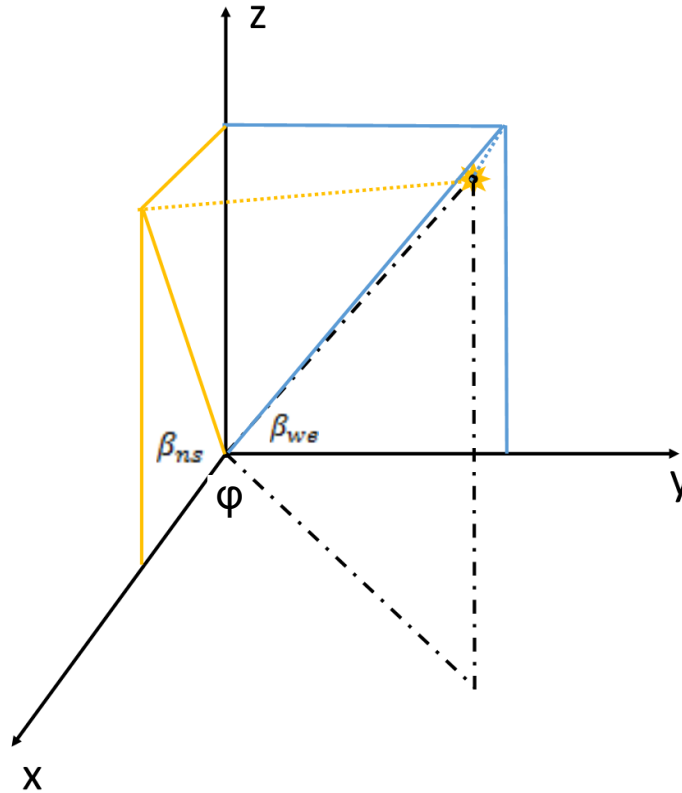


Figure 3-4 Angles β_{ns} and β_{we} in spherical coordinates

Figure 3-4 shows that the two angles β_{ns} and β_{we} are basically the projections of the actual light source on the yz -plane and the xz -plane respectively. In another word, for β_{ns} estimation, the ratio of the signals from the diodes on the North and the South is regardless of the y -axis related information about the light source, similar for the β_{we} . Therefore, if and only if the projection of the light source on the xy -plane is located at the first Quadrant as shown in Figure 3-5, and also the representation of the light source location is (x,y,z) , then the angle φ will be:

$$\varphi = \tan^{-1}\left(\frac{y}{x}\right) \tag{10}$$

and

$$\begin{cases} y = \frac{z}{\tan(\beta_{we})} \\ x = \frac{z}{\tan(\beta_{ns})} \end{cases} \quad (11)$$

Plugging (13) into (12),

$$\varphi = \tan^{-1} \left(\frac{\tan(\beta_{ns})}{\tan(\beta_{we})} \right) \quad (12)$$

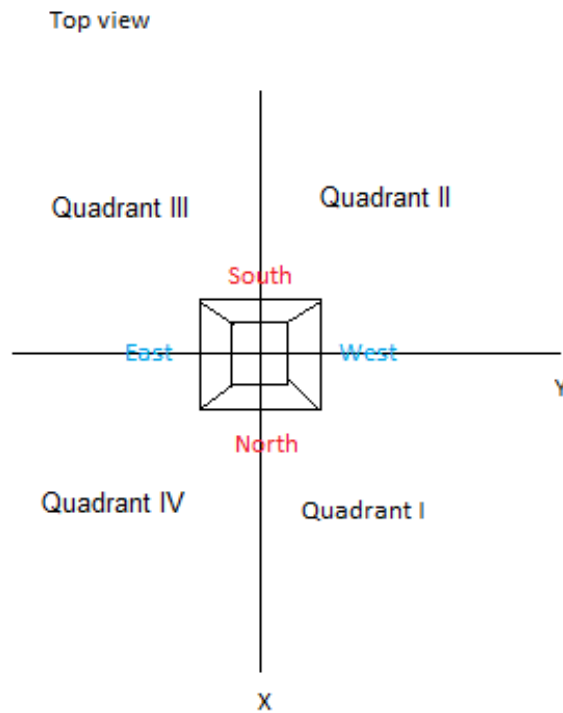


Figure 3-5 Quadrants in XY-plane

However, equation (14) will only satisfy the estimation if both the angles β_{ns} and β_{we} are less than or equal to 90° . Therefore, for the other cases, the reference angle method will be applied from the trigonometry [43]. By the definition, for a non-quadrantal angle in standard position, its reference angle is the actual angle formed by the terminal side of and the horizontal axis. Table 3-1 lists the corresponding reference angles for the actual angles (in the table the angle is called Θ) at all the quadrants:

Table 3-1 Reference angle calculation

Quadrant	Reference angle for Θ
I	Same as Θ
II	$180^\circ - \Theta$
III	$\Theta - 180^\circ$
IV	$360^\circ - \Theta$

The strategy for estimating φ is first to convert the angles β_{ns} and β_{we} into their reference angles respectively, which will be $\beta_{ns_{ref}}$ and $\beta_{we_{ref}}$. The next step is simply plugging these angles into equation (14) by substituting the angles β_{ns} and β_{we} as shown below:

$$\varphi_{ref} = \tan^{-1} \left(\frac{\cot(\beta_{we_{ref}})}{\cot(\beta_{ns_{ref}})} \right) \quad (13)$$

Table 3-2 Algorithm for finding φ

β_{ns}	β_{we}	Quadrant Located	$\varphi =$
$\leq 90^\circ$	$\leq 90^\circ$	I	$\tan^{-1} \left(\frac{\cot(\beta_{we})}{\cot(\beta_{ns})} \right)$
$> 90^\circ$	$\leq 90^\circ$	II	$\pi - \tan^{-1} \left(\frac{\cot(\beta_{we})}{\cot(\pi - \beta_{ns})} \right)$
$> 90^\circ$	$> 90^\circ$	III	$\tan^{-1} \left(\frac{\cot(\pi - \beta_{we})}{\cot(\pi - \beta_{ns})} \right) - \pi$
$\leq 90^\circ$	$> 90^\circ$	IV	$2\pi - \tan^{-1} \left(\frac{\cot(\pi - \beta_{we})}{\cot(\beta_{ns})} \right)$

Finally, the angle φ will be determined based on the information about which quadrant the projection of the light source on the XY-plane is located from the values of the angles β_{ns} and β_{we} .

Table. 3-2 lists the final algorithm of finding the angle φ as an expression of β_{ns} and β_{we} .

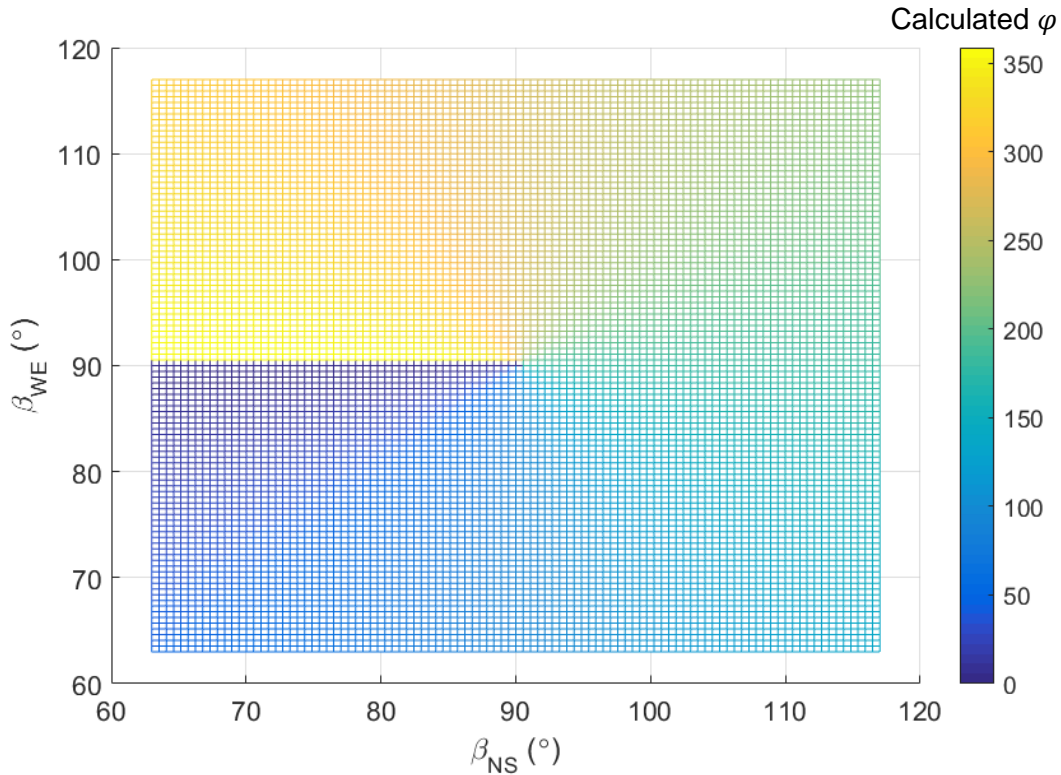


Figure 3-6 Matlab simulation of φ estimation

Figure 3-6 demonstrates the reliability of the algorithm by simulating the result in Matlab. In the simulation the angles β_{ns} and β_{we} are sweeping from 60° to 120° which are the corresponding x-axis and y-axis in the Figure Also the estimated angle φ is shown on the z-axis as the result. As a result, φ is changing from 0° to 360° smoothly and continuously with the changing of β_{ns} and β_{we} .

3.2.2. Estimating the angle θ

The angle θ represents the angle between the arm from the origin through the light source and the z-axis as shown in Figure 3-7. First of all, the expression of the angle θ can be represented by the length of the arm r and the vertical height of the light source z :

$$\theta = \cos^{-1}\left(\frac{z}{r}\right) \quad (14)$$

Neither z nor r are known in the equation. Therefore substitutions for z and r are necessary. By using the definition of the Pythagorean theorem [44], the sum of the areas

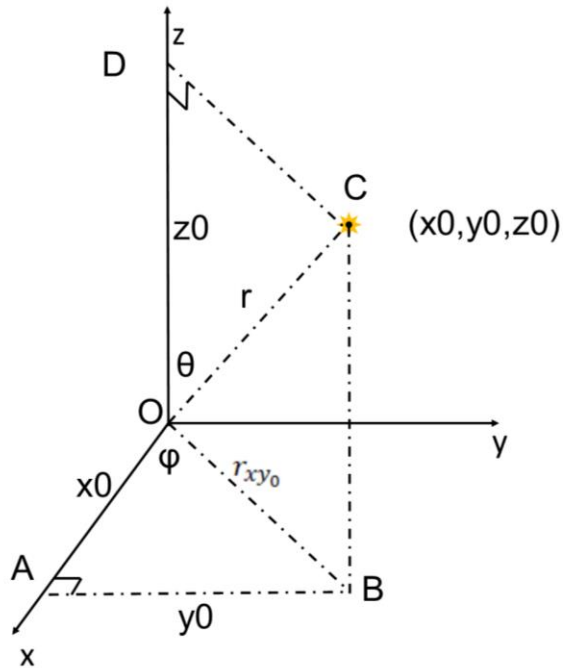


Figure 3-7 Estimating θ by using Pythagorean theorem

of the two squares on the legs (x_0 and y_0) equals the area of the square on the hypotenuse (r projecting on xy -plane, r_{xy_0}). For the right angle OAB,

$$r_{xy_0} = \sqrt{x_0^2 + y_0^2} \quad (15)$$

Moreover, by applying the Pythagorean theorem for the right angle ODC, we have

$$r_0 = \sqrt{r_{xy_0}^2 + z_0^2} \quad (16)$$

Combine equations (16) and (17):

$$r = \sqrt{x_0^2 + y_0^2 + z_0^2} \quad (17)$$

Also, from Figure 3-4, the relationship between x, y, and the angles β_{ns} , β_{we} could be expressed as:

$$y = \frac{z}{\tan(\beta_{we})} = z \cdot \cot(\beta_{we}) \quad (18)$$

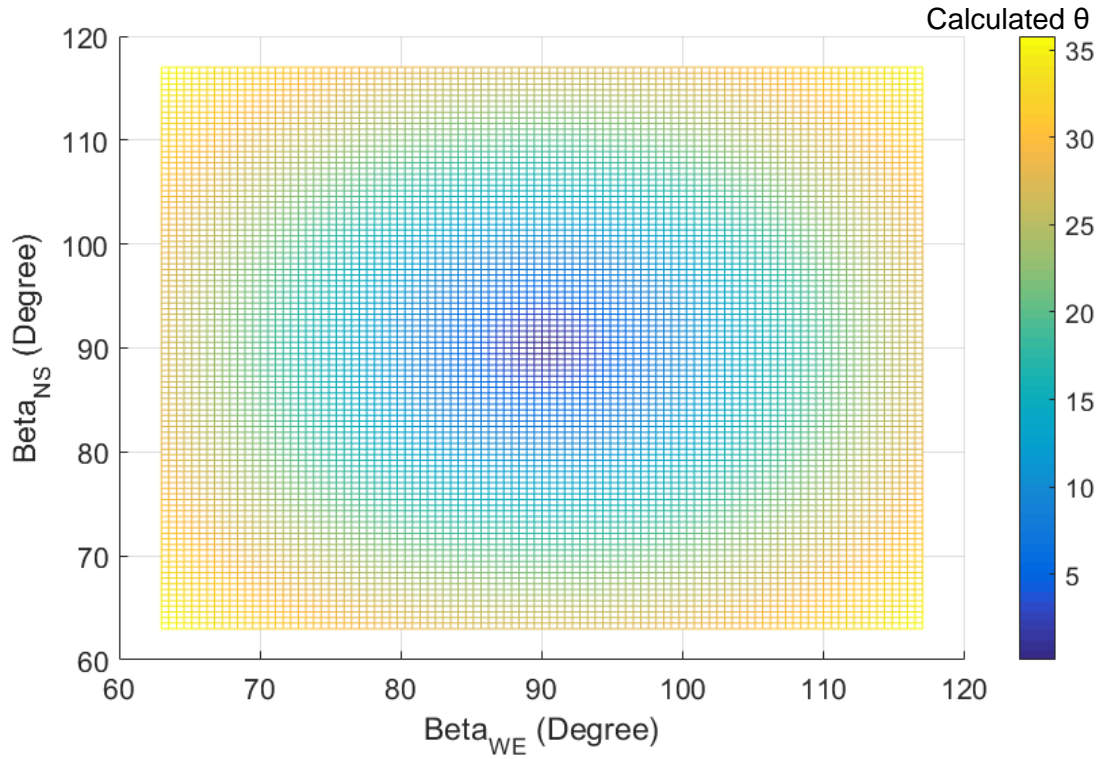


Figure 3-8 Matlab simulation of θ estimation

$$x = \frac{z}{\tan(\beta_{ns})} = z \cdot \cot(\beta_{ns}) \quad (19)$$

Insert equations (20) and (21) to (16):

$$\theta = \cos^{-1} \left(\frac{z}{\sqrt{(z \cot(\beta_{ns}))^2 + (z \cot(\beta_{we}))^2 + z^2}} \right) = \cos^{-1} \left(\frac{1}{\sqrt{(\cot(\beta_{ns}))^2 + (\cot(\beta_{we}))^2 + 1}} \right) \quad (20)$$

Similarly, Figure 3-8 demonstrates the reliability of the algorithm by simulating the result in Matlab. In the simulation the angles β_{ns} and β_{we} are also sweeping from 60° to 120° which are the corresponding x-axis and y-axis in the Figure Also the estimated angle θ is shown on the z-axis as the result. As a result, θ is changing from 0° to 35° smoothly and continuously with the changing of β_{ns} and β_{we} which is the ideal result coming from the physical model.

3.3. Detecting the position of a light source in 3D space

3.3.1. Detecting vertical distance from the sensor of a light source

Based on the finding from previous sections, the direction of a light source could be identified with one pyramid structure. An additional pyramid with a certain distance from the first one could help to find the vertical distance from the light source to the ground level the pyramids sitting. An additional sensor was placed on the y-axis with a distance L from the first pyramid at the 3D coordinate. Figure 3-9 shows the projection of a light source on yz-plane. Since there are two sensors, we call the 2D angles detected by the original sensor β_{we_1} and β_{ns_1} . The angles detected with the same algorithm by the second pyramid were called β_{we_2} and β_{ns_2} . We also define the distance between the original pyramid and the normal line of L through the light source L_1 .

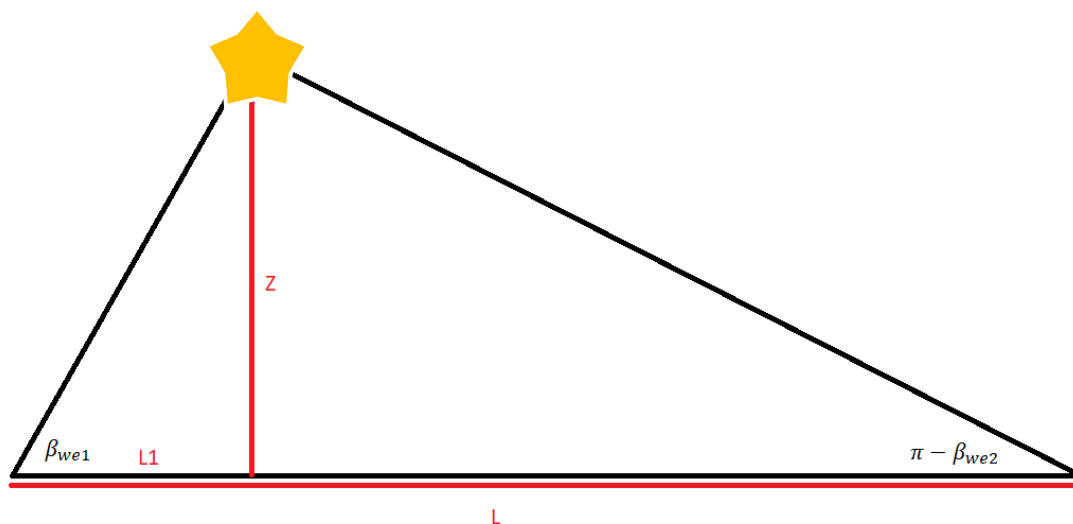


Figure 3-9 Method for finding vertical distance of a light source

From the figure, the relationship between the detected angles, L_1 and L can be:

$$\cot(\beta_{we1}) = \frac{L_1}{Z}$$

$$\cot(\pi - \beta_{we2}) = \frac{L-L_1}{Z}$$

Or

$$L_1 = Z \cot(\beta_{we1})$$

$$Z \cot(\pi - \beta_{we2}) = L - Z \cot(\beta_{we1})$$

Therefore,

$$Z = \frac{L}{\cot(\beta_{we1}) + \cot(\pi - \beta_{we2})} \quad (21)$$

Similarly, if the additional pyramid is placed on the x-axis with a distance L , then

$$\cot(\beta_{ns1}) = \frac{L_1}{Z}$$

$$\cot(\pi - \beta_{ns2}) = \frac{L-L_1}{Z}$$

Or

$$L_1 = Z \cot(\beta_{ns1})$$

$$Z \cot(\pi - \beta_{ns2}) = L - Z \cot(\beta_{ns1})$$

Therefore,

$$Z = \frac{L}{\cot(\beta_{ns1}) + \cot(\pi - \beta_{ns2})} \quad (22)$$

3.3.2. Detecting the position in 3D space

From section 2.2.2, the relationship between the location of a light source in XYZ coordinates and the angles estimated by the original pyramid sensor could be modified from equation (21):

$$\begin{cases} x = z \cot(\beta_{ns}) \\ y = z \cot(\beta_{we}) \\ z = z \end{cases} \quad (23)$$

Substitute equation (23) into (25), finally the coordinate was expressed:

$$(x,y,z) = \begin{cases} \frac{L \cot(\beta_{ns1})}{\cot(\beta_{we1}) + \cot(\pi - \beta_{we2})} \\ \frac{L \cot(\beta_{we1})}{\cot(\beta_{we1}) + \cot(\pi - \beta_{we2})} \\ L \\ \cot(\beta_{we1}) + \cot(\pi - \beta_{we2}) \end{cases} \quad (24)$$

Similarly, if the additional pyramid is placed on the x-axis with a distance L, then

$$(x,y,z) = \begin{cases} \frac{L \cot(\beta_{ns1})}{\cot(\beta_{ns1}) + \cot(\pi - \beta_{ns2})} \\ \frac{L \cot(\beta_{we1})}{\cot(\beta_{ns1}) + \cot(\pi - \beta_{ns2})} \\ L \\ \cot(\beta_{ns1}) + \cot(\pi - \beta_{ns2}) \end{cases} \quad (25)$$

3.4. Inverted pyramid and its mathematical model

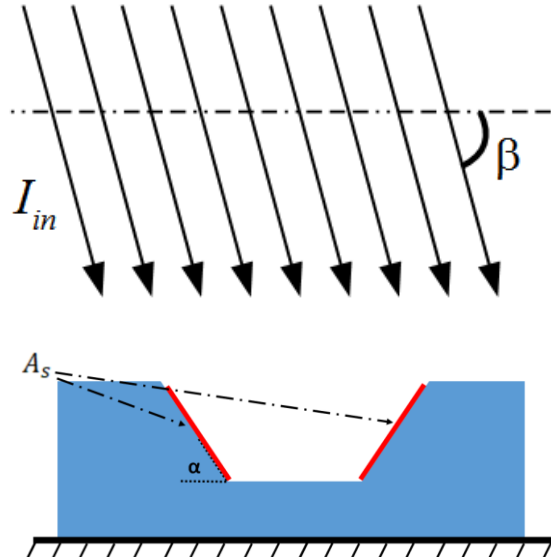


Figure 3-10 Direction estimation in 2D with inverted pyramid

A similar device can be made using an *inverted pyramid* structure (shown in figure 3-10), where the sensors are mounted on the inside walls of a pyramid carved from the

substrate. Similar to equation (4), The powers of light on both photodiodes $P_{l,inc}$ and $P_{r,inc}$ represented by A_s , I_{in} , α and β are:

$$\begin{cases} P_{l,inc} = A_s I_{in} \sin(\beta - \alpha) \\ P_{r,inc} = A_s I_{in} \sin(\beta + \alpha) \end{cases} \quad (26)$$

The ratio between $P_{l,inc}$ and $P_{r,inc}$ is:

$$R_{rl} = \frac{\sin(\alpha+\beta)}{\sin(-\alpha+\beta)} = \frac{I_r}{I_l} \quad (27)$$

Similarly, the estimated β is:

$$\beta = \frac{\pi}{2} - \alpha - \text{atan} \left(\frac{(R_{rl} \cos(2\alpha) - 1)}{R_{rl} \sin(2\alpha)} \right) \quad (28)$$

For angle estimations in 3D and distance estimation, the inverted pyramid shares the same equations with the raised pyramid which were mentioned in section 3.2 and section 3.3.

Chapter 4. Fabrication Process

The VLS structure and operation principle was introduced in section 2.2.4 and Chapter 3 respectively. The macro-model prototype was fabricated and tested successfully as mentioned in the previous chapter. This chapter is about miniaturization with the motivation coming from the pyramid structures that can be easily created on silicon and mass-manufactured.

4.1. Microfabrication steps

The vector light sensor (VLS) is fabricated through a combination of four pn-junctions on a pyramid 3D structure created by potassium hydroxide etching of a silicon wafer. The main steps for the procedure will be the following: 1) Silicon etching for 3D pyramid structure, 2) N-type dopant implantation, 3) metallization and 4) Packaging. The fabrication process was completed in the cleanroom in Engineering Science department and the one in 4D Labs at Simon Fraser University. Figure 4-1 demonstrates the most critical procedures of the fabrication.

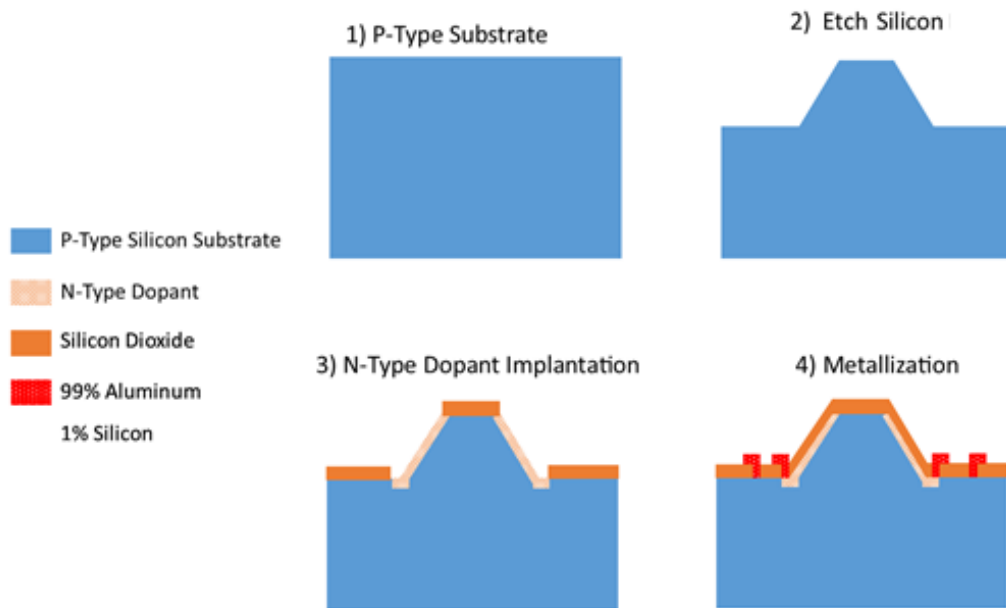


Figure 4-1 Main steps for the device fabrication. Note that passivation steps are skipped for brevity.



Figure 4-2 3D Structure Device Simulation

As shown in the above, the process started with a plain P-type wafer. Silicon dioxide was created uniformly as a mask layer for silicon etching. After the 3D silicon structure was etched, all the oxide was etched away, and a new layer of oxide was grown for N-type doping patterns. Similarly, the oxide mask was etched after the dopant were implanted through the opening surface. The dopants are activated during a subsequent oxidation step, achieving the same function as annealing. The third lithography step was to create an opening for contact vias. The fourth lithography then was for metallization (lift-off). All the oxidation procedures were done at the Engineering Science cleanroom, the rest of the fabrication process was completed inside 4D Labs. The four chromium masks for lithography were designed using CoventorWare 10.2 and manufactured at 4D Labs. Four masks were created by CoventorWare Layout Editor which are named Pyramid Mask, Doped Mask, Vias Mask, and Metal Mask respectively. Figure 4-2 shows the 3D structure of the device by using the process simulation with CoventorWare Solid Model Builder. The size of the trench was designed to be $100\mu\text{m}$ by $100\mu\text{m}$. The height difference between the metal surface and the etched trench is $20\mu\text{m}$. The sensitive region will be on the $\langle 111 \rangle$ planes which side walls of the inverted pyramid as shown in Figure 4-2. Details of each process step will be mentioned in the following sections and Appendix A.

4.2. Fabrication steps

4.2.1. P-type silicon substrate selection

To create a pyramid structure by using silicon wet etchant, a silicon wafer with $\langle 100 \rangle$ is required. Base on the mechanism of KOH etching of silicon $\langle 100 \rangle$ surface [41], $\langle 111 \rangle$ planes will be created as side walls of the inverted pyramid structure which is 54.78°

with the surface. The other main concern is the initial dopant of the wafer itself. Since P-type substrate is used for the device, prime silicon wafer with Boron as the dopant was chosen. The wafer was picked with 0.1 – 0.2 Ohm.cm resistivity. Table 4-1 shows the main parameters for the selected silicon wafer.

Table 4-1 Specifications of a silicon wafer provided by the manufacturer

Diameter	Type/ Dopant	Resistivity	Orientation	Thickness	Surface/Back Side
100±0.5mm	P/Boron	0.1-0.2 Ohm.cm	<100>±0.5 deg	525±25 μm	Polished/ Lapped, Etched

1) P-Type Substrate



2) Thermal Oxidation



3) Spin photoresist



Figure 4-3 Fabrication process steps: Thermal oxidation and photoresist deposition

4.2.2. Thermal oxidation

The silicon substrate was patterned and etched by KOH and TMAH solutions for the pyramid structure. During the etching, silicon dioxide will be the mask on top of the silicon surface. Therefore, initially, a layer of high-quality silicon dioxide was uniformly formed by thermal oxidation with the furnace in the cleanroom from the school of Engineering Science. The desired oxide thickness for the mask was 550nm based on the etching rate of KOH for both silicon and silicon dioxide. Before the oxidation procedure, standard RCA-1 and RCA-2 cleaning were performed on the plain wafer. Wet oxidation was operated at 1100°C for 55 minutes in order to grow 550nm oxide [45],. The color of the wafer surface turned into dark green. By reading the silicon dioxide table [46], the thickness was estimated as 550nm. The thickness of the silicon dioxide was measured by reflectometer in 4D Labs as 530nm.

4.2.3. Lithography for mask #1

Figure 4-3 and figure 4-4 shows the steps creating the oxide mask for etching silicon. After the oxidation, AZ-703 photoresist was used as the UV light-sensitive material. That is, the area exposed to UV light will be sensitive to the developing solution and will be stripped off from the deposited area. Before depositing the photoresist, HMDS was spun on the surface to improve the adhesion between the surface of the silicon dioxide and the photoresist [47]. A few drops of the HMDS solution in a container was placed next to the silicon wafer inside the HMDS chamber under vacuum for 5 minutes. Following the recipe from the AZ703 User Manual, the photoresist was deposited on the surface with the spin coater at 3000 rpm for 60 seconds [48]. The transparent part of the mask will allow the substrate to be exposed under the UV light so that the photoresist will be removed by AZ300 developer. A post exposure bake was done at 110°C for 1 minute to make the unexposed photoresist more resilient during the development process. The exposed wafer was placed in the developer for 60 seconds with constant agitation. The completed developed photoresist mask is now ready for oxide etching. Moreover, the thickness of the photoresist was measured as about 1um with profilometer by scanning across the un-stripped and stripped photoresist areas.

4.2.4. Etching the oxide layer

A post-development bake was done at 110°C for 1 minute to increase the sustainability of the photoresist mask during the SiO_2 etching process. The etching rate for silicon dioxide with the BOE solution was calculated by 4D Labs staffs as 6.5Å/s. The wafer was dipped into a buffered hydrofluoric acid for 9 minutes and 30 seconds (with 20% over etching required) to etch away the oxide on the open area. During the oxidation process, both front and back sides of the wafer were oxidized. Therefore, the oxide etching would be complete if the back side of the wafer was hydrophobic. At the end, the photoresist was stripped by acetone and rinsed in IPA.

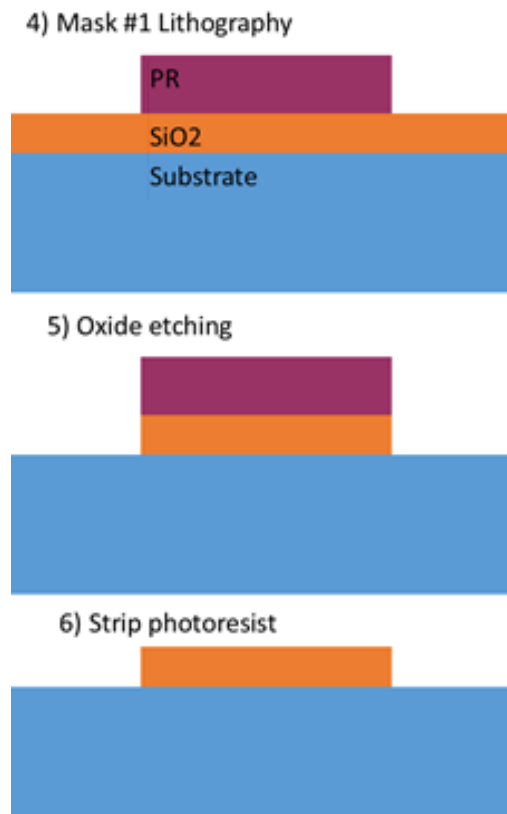


Figure 4-4 Fabrication process steps: Thermal oxidation and photoresist deposition

4.2.5. Etching the substrate

Figure 4-5 shows the steps etching the silicon substrate. The wafer was placed into 865ml of 30% KOH solution diluted with DI water. The solution was heated to 80°C,

7) Silicon anisotropic etching



8) Oxide etching



9) Wet oxidation

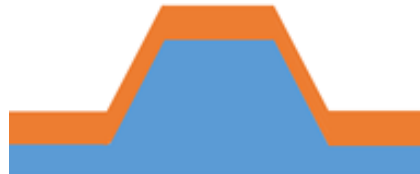


Figure 4-5 Fabrication process steps: Silicon etching, oxide etching and oxidation

then 150ml of IPA was added into the solution. The solution was stirred with a magnetic spinner. After the wafer was under the solution for 20 minutes, it transferred to the TMAH solution at 90°C for 3 minutes. TMAH has much lower etch rate than KOH[49]. However, the reaction is much more moderated. Finishing the etching process with TMAH etchant resulted in a smoother surface on the device. After the TMAH etching, the height of the pyramid created was measured by profilometer as 20.5 μm . All the recipes for KOH and TMAH etching were optimized by using a test wafer before the main wafer was proceeded. Appendix A describes all the critical parameters for the silicon etching process with KOH and TMAH solutions. After the etching process with both solutions, the wafer was rinsed in DI water for 3 minutes. At the end, all the silicon dioxide was stripped by BOE for 9 minutes and 30 seconds, and both sides of the wafer were observed to be hydrophobic. After the oxide was etched, the valley was scanned under profilometer, and the depth of the valley was 20 μm .



Figure 4-6 Spray coater

4.2.6. Oxidation for Mask #2

A same thermal oxidation procedure as section 3.1.2 was repeated to create the oxide mask for the second lithography.

4.2.7. 3D lithography for Mask #2

Since there are 20um trenches everywhere on the surface of the wafer, the spin coating will not be a feasible option to deposit photoresist anymore. The structures on the wafer will break the uniformity by blocking the photoresist traveling from the center to the side of the wafer during its spinning. Therefore, a spray coating method will be applied with the spray coater in 4D Labs (Figure 4-6). This process needed a significant amount of trial and error to produce repeatable results as described in section 4.4. An HMDS priming was done for 5 minutes before the spraying. The photoresist was still AZ-703 but it was diluted 1:1 with solvent. The solution was transferred to a syringe and connected to the nozzle of the spray coater through the tube. Six layers of photoresist were sprayed on the wafer, three scanned vertically and three horizontally. The detail of the recipe is provided in Appendix A. After the procedure, the wafer was baked on a hot plate at 90°C for 5 minutes. The reason for increasing the time of the soft bake is to make sure that all the solvent is evaporated from the wafer.

The wafer with the photoresist was then exposed with the second designed mask under the UV light for 30 seconds. After that, the wafer was baked on the hot plate at 110°C for 5 minutes. The photoresist on the area exposed to UV light is then stripped with the same developer for 120 seconds. Since the troubleshooting and optimization of the recipe for this 3D lithography were complicated, the detail will be mentioned in the

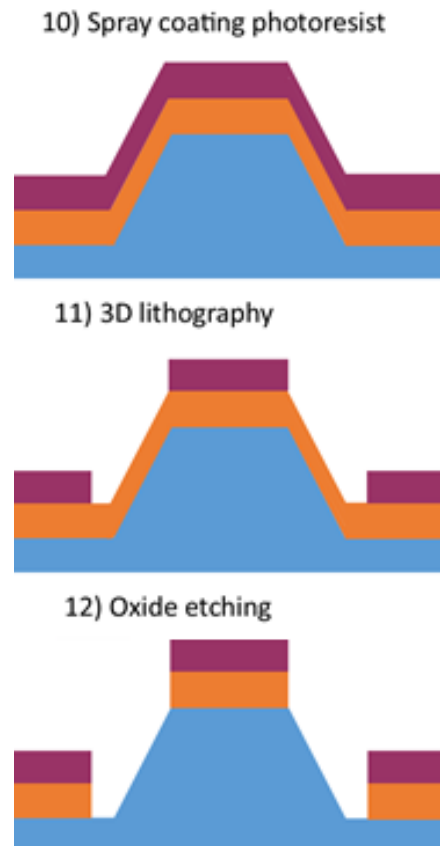


Figure 4-7 Fabrication process: 3D lithography for Mask #2

upcoming section. Once the photoresist pattern was created, the same BOE etching procedure from section 3.1.4 was performed for the wafer. In the end, an oxide mask with the desired pattern was completed and it the wafer was ready for the N-type dopant ion implantation. Figure 4-7 shows the step creating the oxide mask for N-type doping area with 3D lithography technique.

4.2.8. Pre-implant Oxidation

To ensure that all the PN-junctions are as similar as possible, tilting should not be done during the ion implantation. However, we need to prevent the channeling effect [50]. Therefore, a thin layer of oxide was grown on top of all opening. Wet oxidation was done at 800°C for 40 minutes to create 20nm oxide.

4.2.9. N-type dopant ion implantation

The wafer was cleaned by RCA-1 and RCA-2 again to ensure that the surface is clean and ready for the implantation. The depth and profile of doped regions impact the device performance significantly. It is, therefore, necessary that these parameters are determined according to the device requirements. For this work, we decided to have junctions that were about 0.5µm below the surface to isolate them from the surface effects. Figure 4-8 shows the steps for N-type dopant ion implantation.

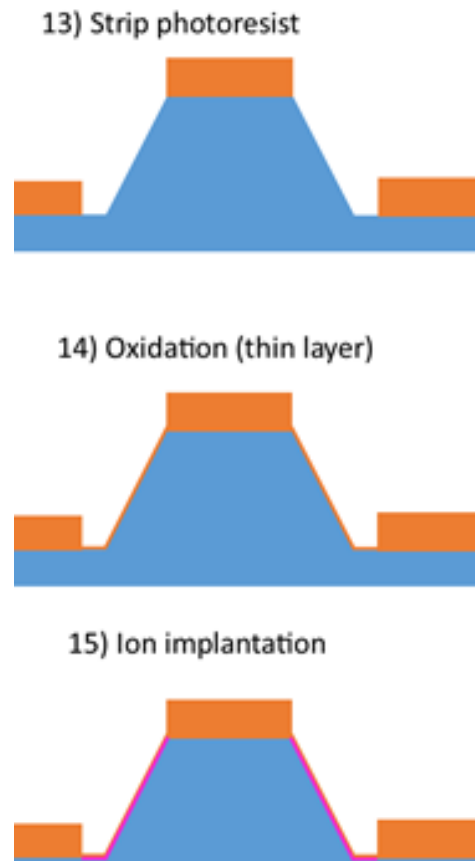


Figure 4-8 Fabrication process: Ion implantation

Doping parameters

The recipe was optimized by doing a simulation with Synopsys to get the desired PN-junction depth for about 300nm on the <111> walls. After the implantation, all the oxide was etched by following the same procedure in section 3.1.4.

The final dopant implantation parameters were:

First implant: Dose = 1.2×10^{12} ions/cm², Energy – 20keV, Tilt: 0

Second implant: Dose = 4×10^{14} ions/cm², Energy – 10keV, Tilt:0

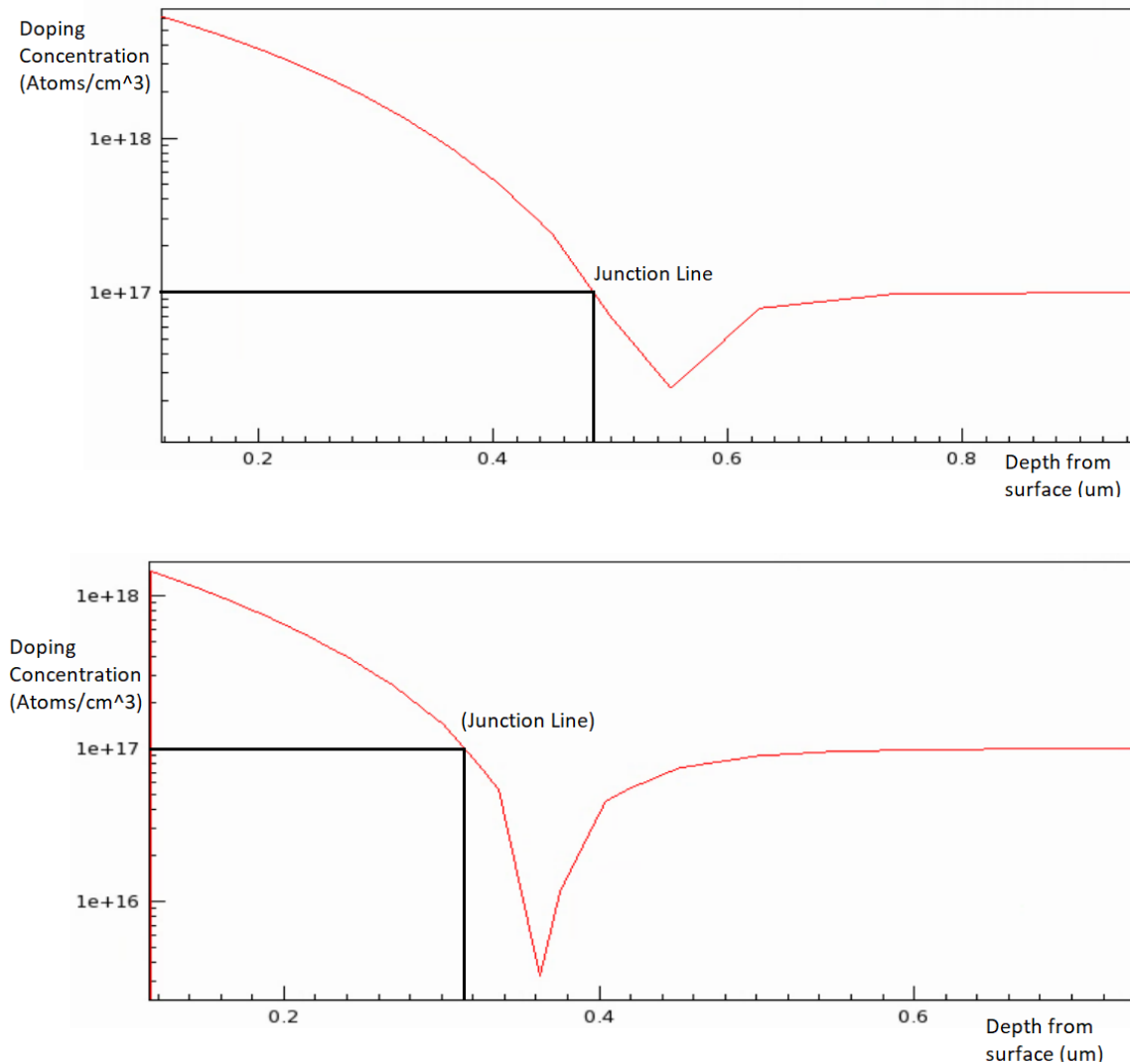


Figure 4-9 Simulation of doping profile on the flat silicon surface (top) and on the side walls (bottom)

Figure 4-9 shows the simulation results on the <100> and <111> planes with the above parameters. Since the <111> plane has 54.75° angle with the flat silicon surface, it will have a shallower junction than the doped region on the flat silicon surface. As we could see from figure 4-9, the junction depth of the N-type doped region was 500nm on the <100> plane, meanwhile, the junction depth on the <111> plane was about 300nm.

4.2.10. Oxidation/ Annealing

Since ion implantation process involves the collision of high energy ions with the atoms of the substrate, the structure of the silicon will be damaged. Therefore, an annealing procedure is necessary to recover the silicon crystal as well as to activate the electrical property of the PN-junctions [51]. Moreover, a layer of oxide is needed for the separation between the electrical access of the N-type doping and the P-type doping. Also, the oxide layer could protect the devices from electrical leakage.

Therefore, low-temperature wet oxidation was operated on the wafer. At the same time, the PN-junctions were also activated. The wafer was inside the wet oxidation furnace at 900°C for 2 hours. The thickness of the oxide created was 200nm measured by the reflectometer.

4.2.11. 3D lithography for Mask #3

The purpose of the via mask is to create the access points for the metal pad to both the n-type region p-type regions. The vias for each area was made by small holes in a matrix or an array. Figure 4-10 and Figure 4-11 shows the microscope captures for both inverted pyramid and raised pyramid respectively. As we can see, there is a chance that some of the holes were blocked during the developing process. Therefore, the more holes created in the region, the better the region was secured to gain a connection to the metal. Figure 4-12 shows the steps during the 3D lithography for mask #3.

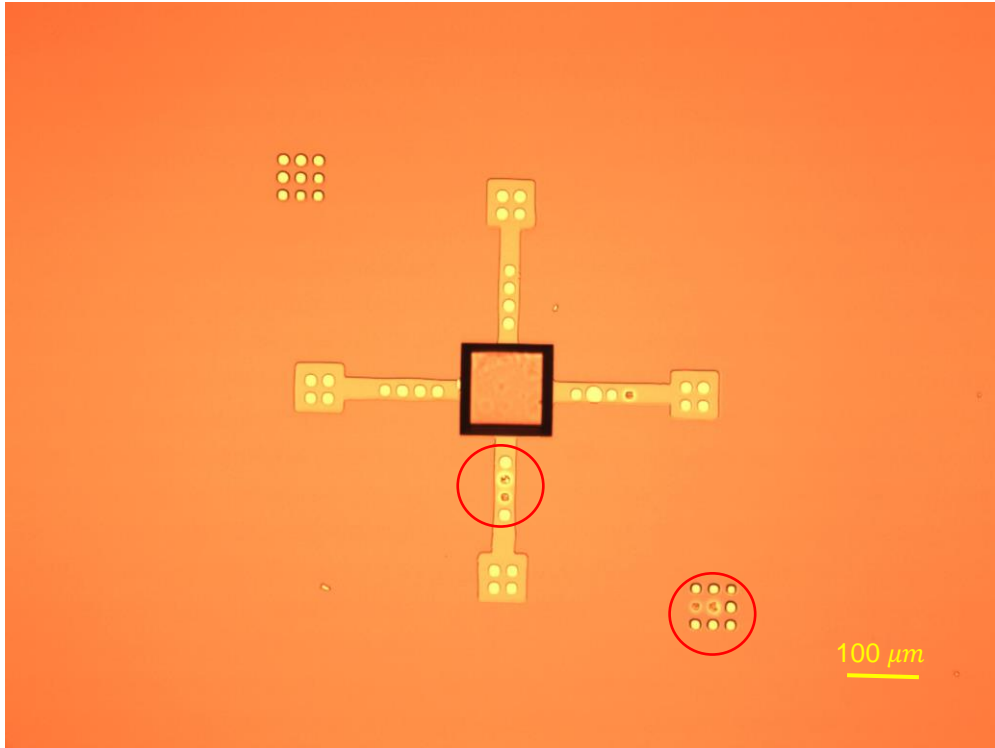


Figure 4-10 Microscope screenshot of inverted pyramid after Mask #3 3D lithography

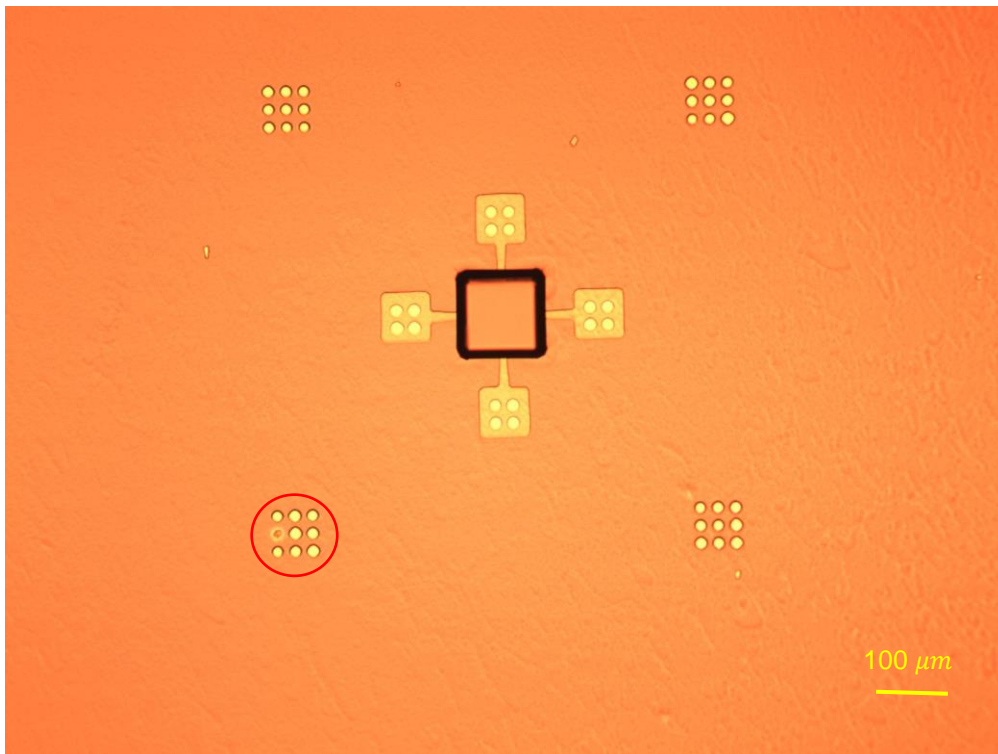


Figure 4-11 Microscope screenshot of raised pyramid after Mask #3 3D lithography

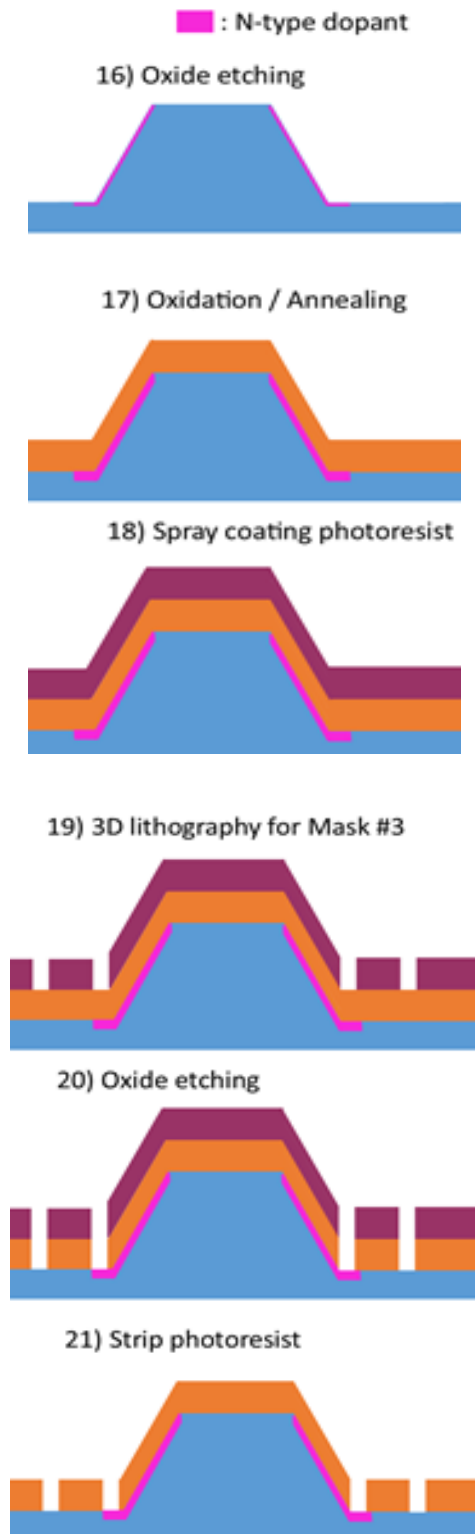


Figure 4-12 Fabrication process: 3D lithography for Mask #3

4.2.12. Metallization

Metallization was the step to deposit Aluminum on top of the silicon dioxide. The metal will connect both the n-type region and the p-type region with the routings on the oxide layer. Pads with the relatively more significant area will also be created on the oxide layer for testing with probes or wire bonded packages. This procedure includes 3D lithography for the Mask #4, metal deposition with evaporation method and photoresist lift-off. The 3D lithography was completed by following the same process as the one for Mask #2. The purpose of the 3D lithography is creating the pattern for the metal layer for testing. After the photoresist mask was patterned, 300nm of Al99Si1 was deposited on the wafer with an evaporator in 4D Labs. In the end, the photoresist was lifted-off using acetone with sonicator in 4D Labs.

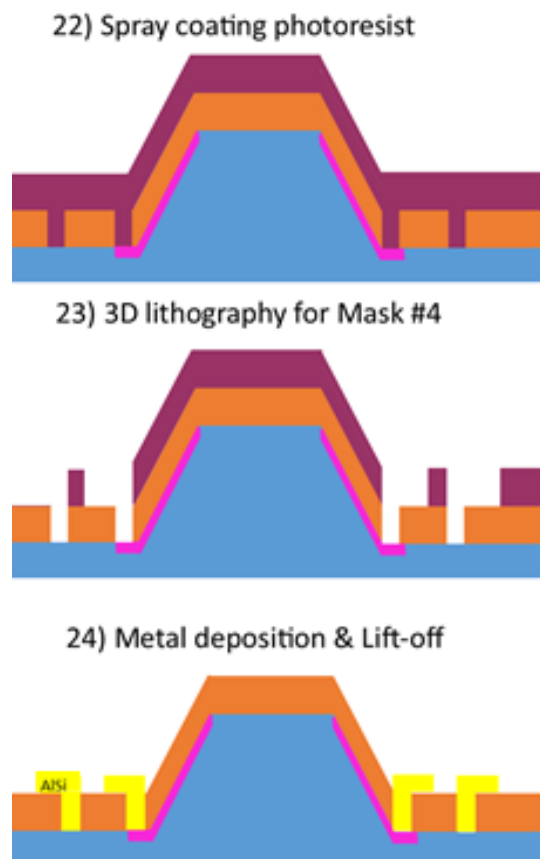


Figure 4-13 Fabrication process: Metallization

Figure 4-13 step 24) was the last step for the fabrication process. Figure 4-14 shows the image of the completed wafer after metallization.

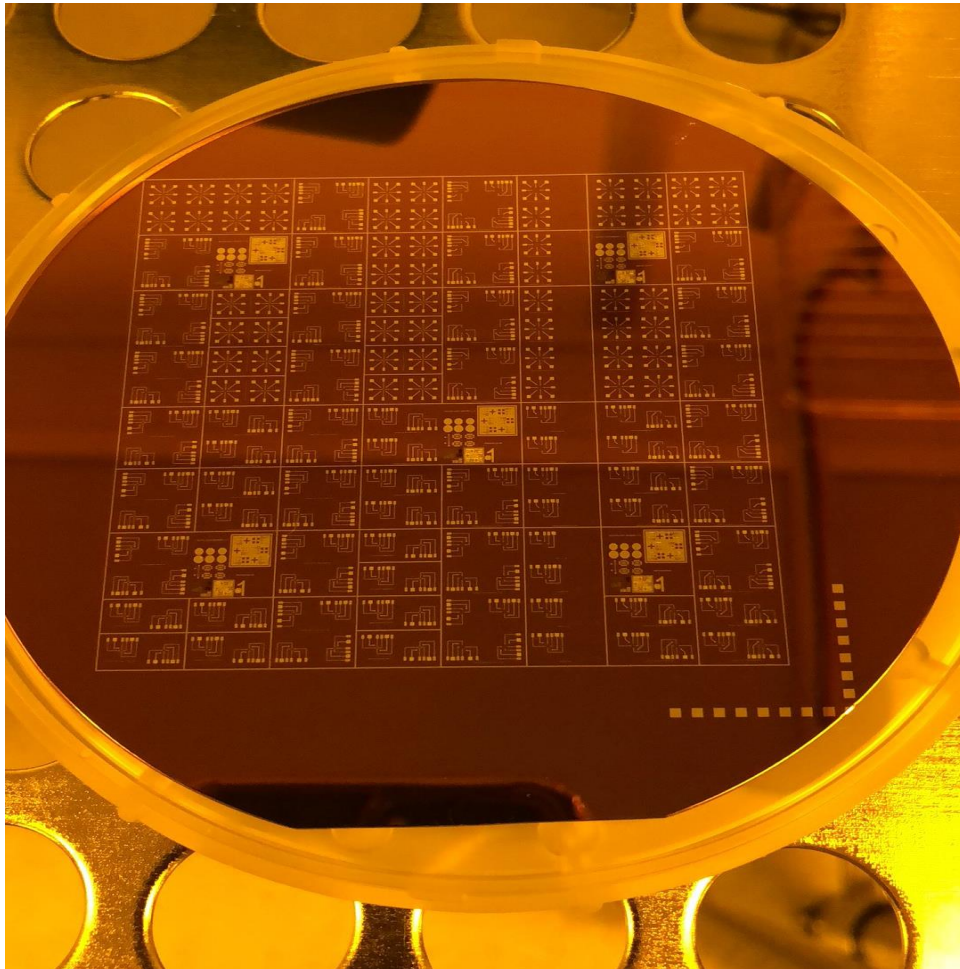


Figure 4-14 Picture of the wafer after lift-off

4.2.13. Packaging

Following the metallization process, some of the diced chips with VLS devices should be packaged for characterization purpose. Each chip was mounted inside a Dual-In-Line ceramic package (DIP). After that, electrical wiring between metal pads and external components was performed by wire bonder. Figure 4-15 was a read- to-test package with 4 VLS devices. Details of relevant parameters to control the wire bonding device is shown in Appendix.

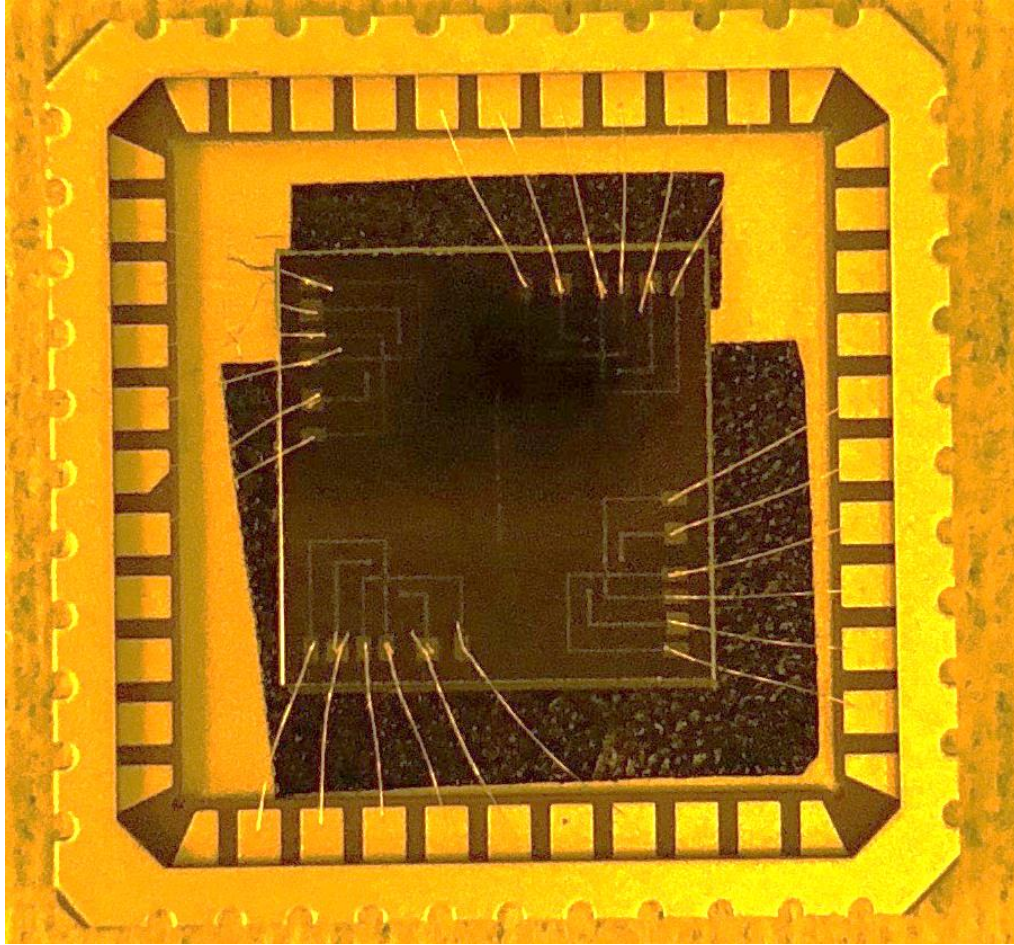


Figure 4-15 Wire bonded package

4.3. Corner compensation for raised pyramids

To etch the three-dimensional pyramid structure, the silicon substrate was etched in a basic solution (e.g., in KOH). With proper mask design, the vastly different etch rates for different crystal directions can be employed to etch the pyramid from the substrate. In particular, we took advantage of the large selectivity of KOH and TMAH to etch $\langle 100 \rangle$ planes compared to $\langle 111 \rangle$ planes (up to 100:1 selectivity for $\langle 100 \rangle$: $\langle 111 \rangle$ planes if KOH is used). To create a raised pyramid with sharp corners, different additional structures need to be added to the basic layout [52]–[54]. The etching for inverted pyramid structure, on the other hand, is straightforward as long as the sidewalls are properly aligned to expose the $\langle 111 \rangle$ planes on the sides of the structure. The inverted pyramid has four

concave corners, formed by four $\langle 111 \rangle$ sidewalls. In this case, each corner is nicely shaped, and no corner compensation method is needed for this structure.

On the other hand, for raised structure, undercutting at the convex corner [55] is occurred during the wet anisotropic etching. To create nice and smooth convex corners, square-shaped was used to compensate. Figure 4-16 shows the design for 20um height raised structure. Squares for compensating were at the corners of the main structure. The dimension of the square was designed to be double the height of the raised structure.

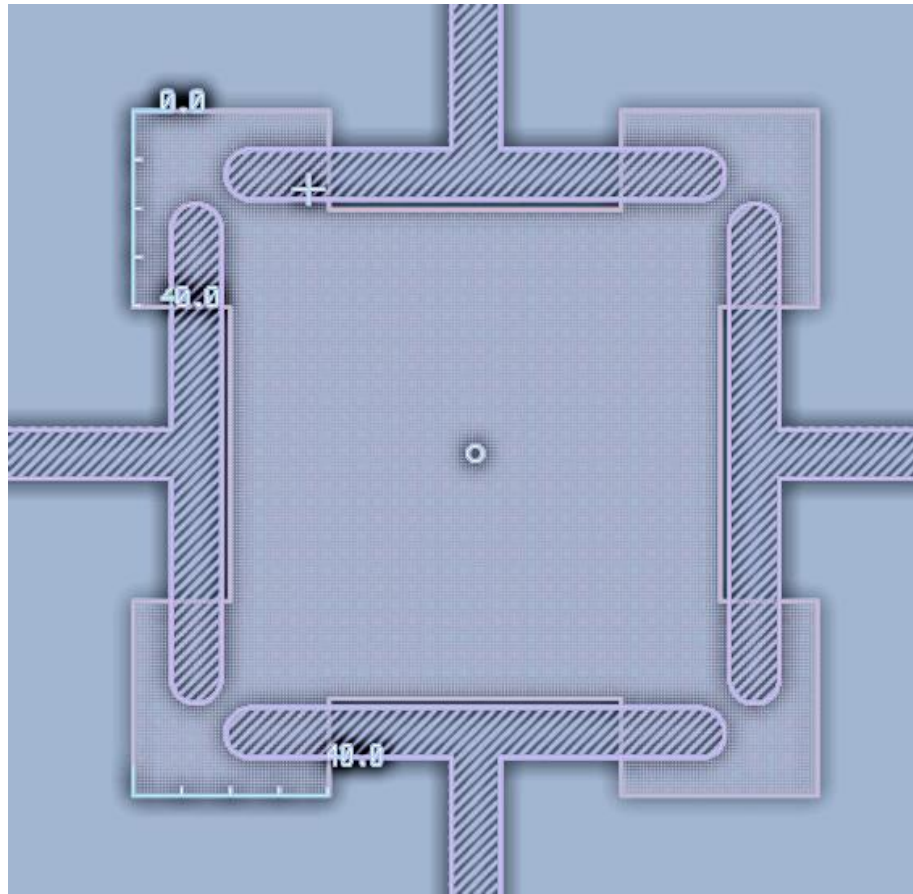


Figure 4-16 Square-shaped design for compensating structures

There were three different designs for raised structures in the same wafer with different heights: 20um, 60um, and 100um. Therefore, three different wafers were used with varying lengths of time for wet anisotropic etching. As a result, on the wafer with etching for 20um, the structures for 60um and 100um were not pyramids with perfect convex corners. Figure 4-17 showed the raised structure designed for 60um but etched

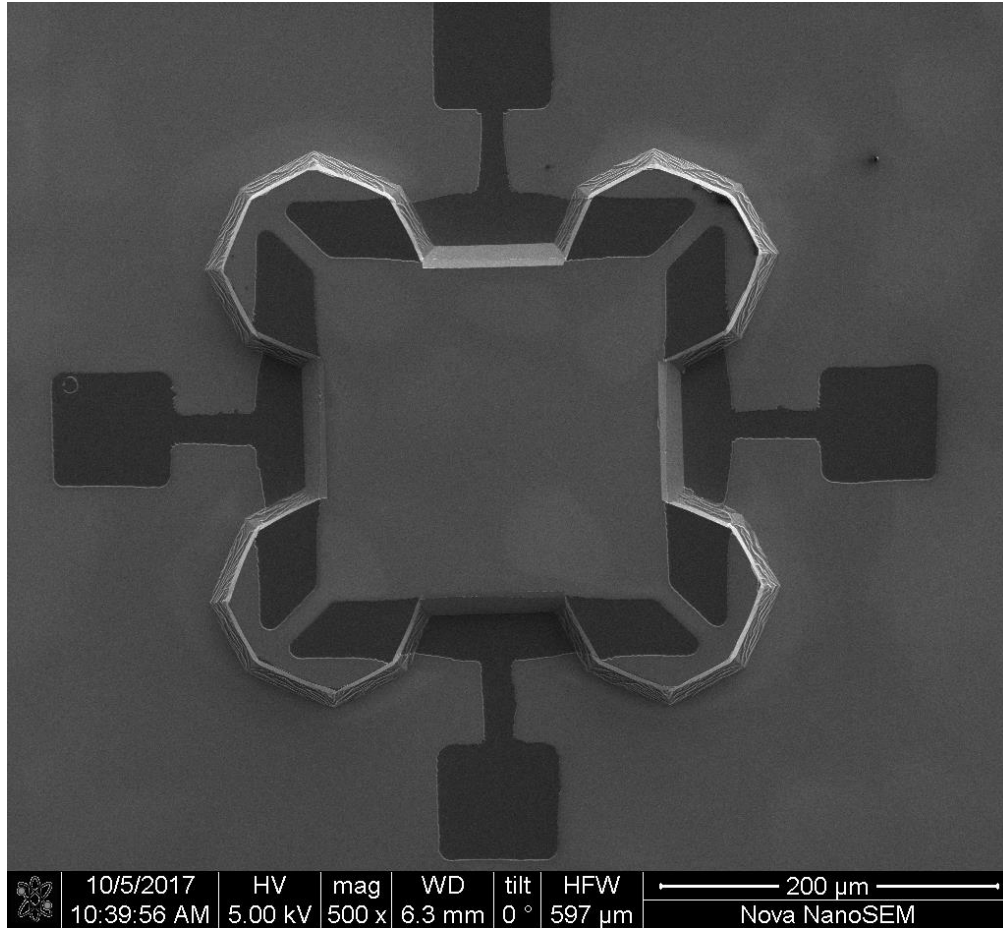


Figure 4-17 Raised structure designed for 60um with 20um height

for 20um. Moreover, Figure 4-18 showed the raised structure designed for 60um and etched with 60um as well. As a result, the square-shaped corner compensation design efficiently created smooth convex corners for raised structures.

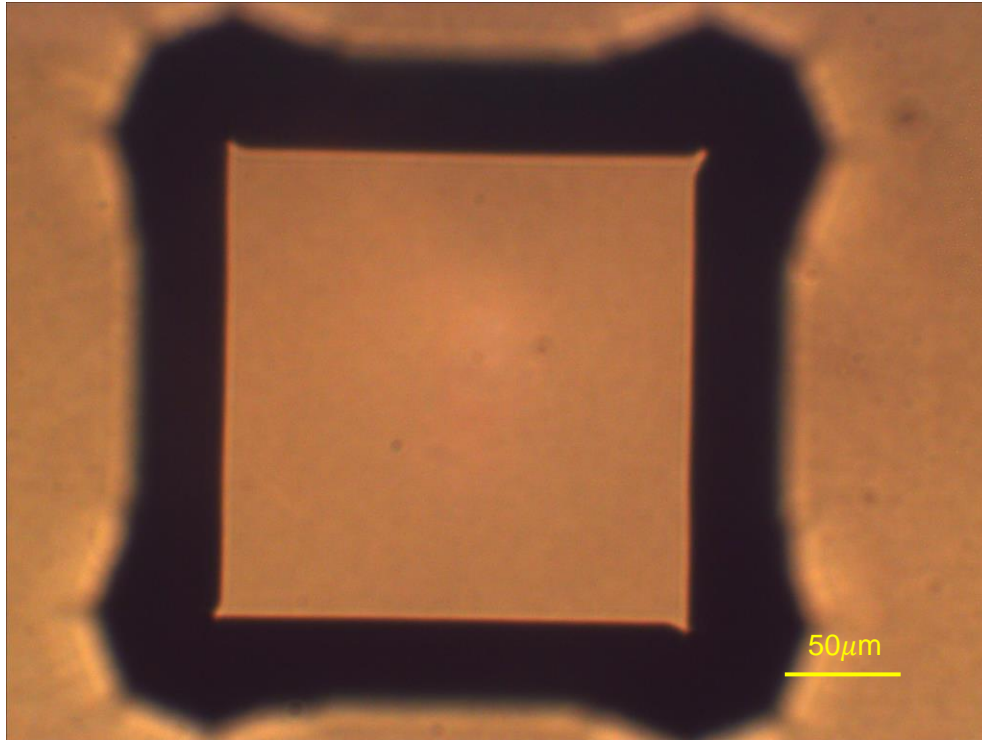


Figure 4-18 Raised structure designed for 60um with 60um height

4.4. Optimization of 3D lithography

In this section, an optimization with a few essential parameters for the 3D lithography procedure was performed:

- *Thickness of photoresist*
- *Exposure time*
- *Developing time*
- *Baking conditions*

Soft bake recipe after spray coating, hard bake recipe after exposure, developing time, and post-development bake recipe are easier procedures to change parameters and to optimize.

Soft bake of photoresist [49] was done after photoresist deposition. The photoresist is baked to drive off solvents and to solidify the film. Soft bakes are commonly performed on hot plates, and typical temperatures range from 90 to 110°C. The reason why the process needed to be optimized is the high thickness of the photoresist deposited on the wafer. The higher the temperature of the soft bake, the more robust the photoresist will be. However, the evaporation rate of the solvent cannot be too rapid. Otherwise it will cause bubbles on the surface. Figure 4-19 shows a microscope image of a surface with bubbles produced by the missing time for the soft bake. Also, soft bake must be done right after photoresist deposition to prevent the solvent from drying. The solution for this issue was to lower the temperature to 90°C but increase the baking time to 5 minutes.



Figure 4-19 Post development silicon wafer surface with bubbles

The next important procedure was an additional photoresist bake after exposure or post exposure bake (PEB). A PEB will help smooth rough feature sidewalls caused by standing waves characteristic of thin film interference in a monochromatic exposure process [57]. A PEB process is essential before developing the photoresist. Without PEB the resist would not develop or only be developed at a meager rate.

Since the smallest resolution in this fabrication process was 10um, over developing the exposed area was allowed and necessary to ensure such a thick layer of photoresist would be able to be removed. Moreover, even though with perfect developing time and an ideal result for the inverted pyramid, it might not be an excellent result for the raised pyramid. Because the spray coating photoresist on the wafer was relatively too thick, and during the deposition, a lot of photoresists was accumulating at the bottom of the side walls of the raised pyramid. However, if the wafer was too much overdeveloped, the primary issue will be a short circuit between the opening of side walls.

4.5. Ion implantation vs. diffusion

The first batch of the fabricated devices was tested by Keithley 2400 source measure unit (SMU) and probe station. Unfortunately, most of the IV characteristic graphs of the diodes in the devices shows linearly increasing high leakage current in the reverse-

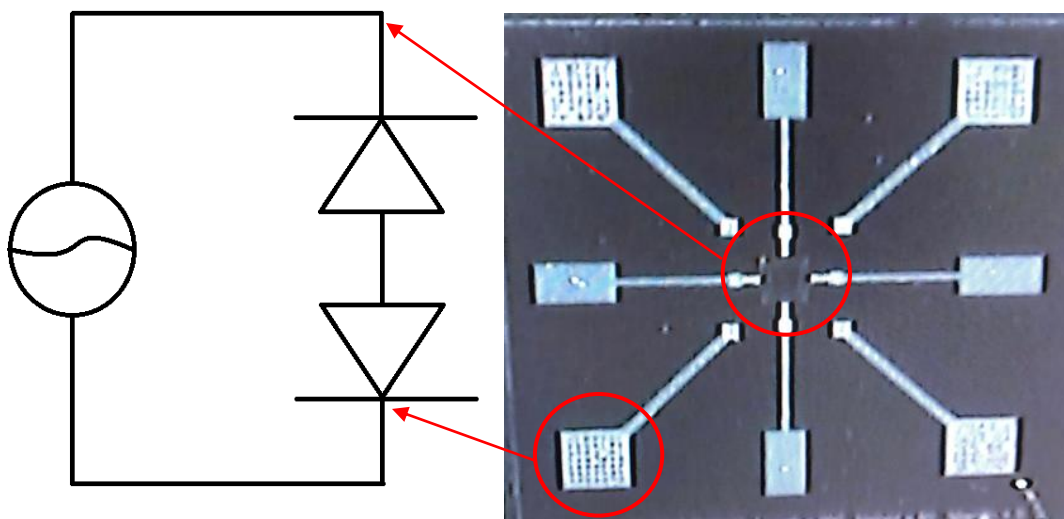


Figure 4-20 Voltage sweep between two N-regions of neighbor diodes

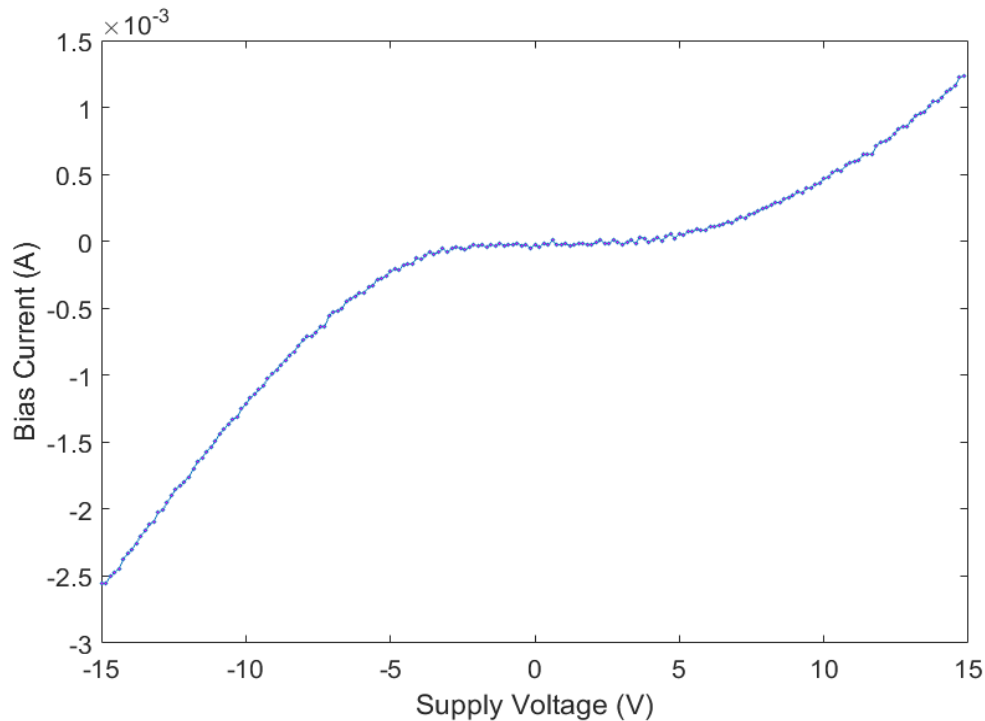


Figure 4-21 IV plot for voltage sweep between two N-regions of neighbor diodes

bias region moreover, if we probe two neighbor diodes in series and sweep the supply voltage from -15V to 15V as followed in figure 4-20, the current responded similarly as an ohmic contact which was not expected.

Figure 4-21 indicates the current response with the voltage sweeping from -15V to 15V. The reactions were similar with the connections between the N-regions on the opposite facets.

We suspected that some issues occurred during the ion implantation process. It was possible that N-regions were not firmly separated from each other because of the implantation energy. Eventually, we decided to start a second fabrication run. The process flow of the second fabrication run was identical to the first run except for using the diffusion method instead of ion implantation. The diffusion recipe was copied from the previous grad students in Intelligent Sensors Laboratory which is:

- Phosphorus diffusion: 975°C for 30minutes

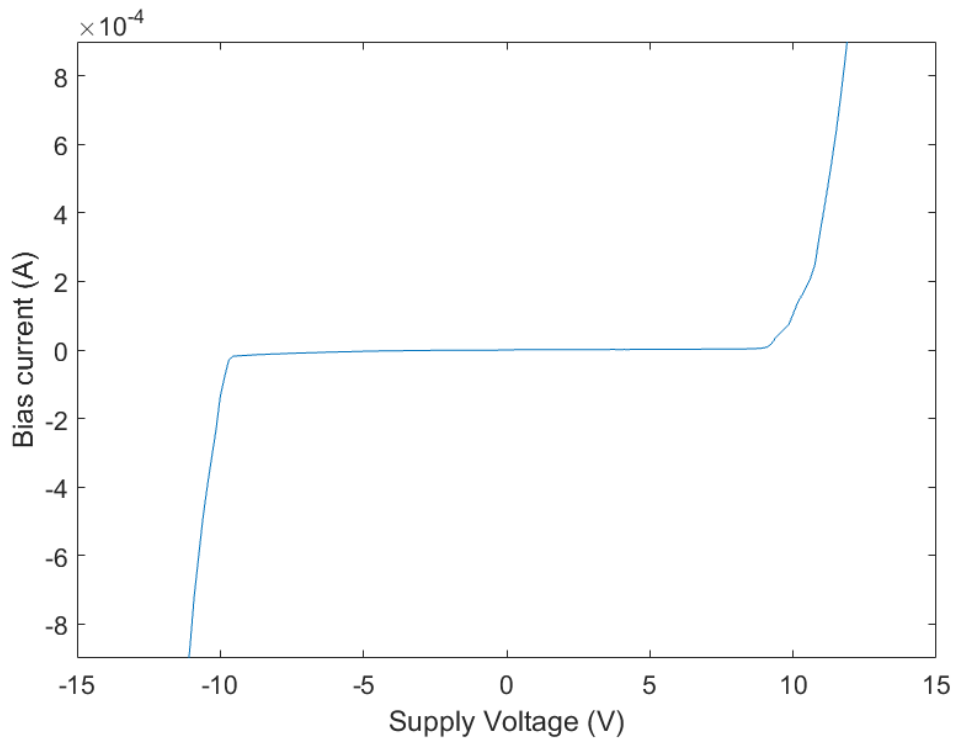


Figure 4-22 IV plot for voltage sweep between two N-regions of neighbor diodes with a diode from the second fabrication run

- Low-temperature Oxidation: 800°C for 3 hours

Based on the recipes developed by Amin Rasouli, a secondary ion mass spectrometry (SIMS) was completed on the doped area from the above recipe [58]. From the SIMS, it could be expected that the junction depth would be about 1 μ m.

The new devices were tested again by sweeping the voltage from -15V to 15V between two N-region. The result shows in figure 4-22 as followed:

Significant enhancement was achieved from the second fabrication run. The breakdown voltages for both the diodes were about -10V. The reverse-bias current before breakdown was about 10 μ A.

4.6. SEM images for devices

Figure 4-23 shows an SEM image for a raised pyramid designed with 20um height. The contrast difference separated the doped region and undoped region. The smallest distance between the two doped regions at the corner of the pyramid was 3.36um. The purpose of the measurement was to ensure that doped regions would not connect. Figure 4-24 is a zoomed-in image for a closer look at the corner. The substrate was tilted 30° towards the camera.

Similarly, Figure 4-25 shows the SEM image for completed inverted pyramid.

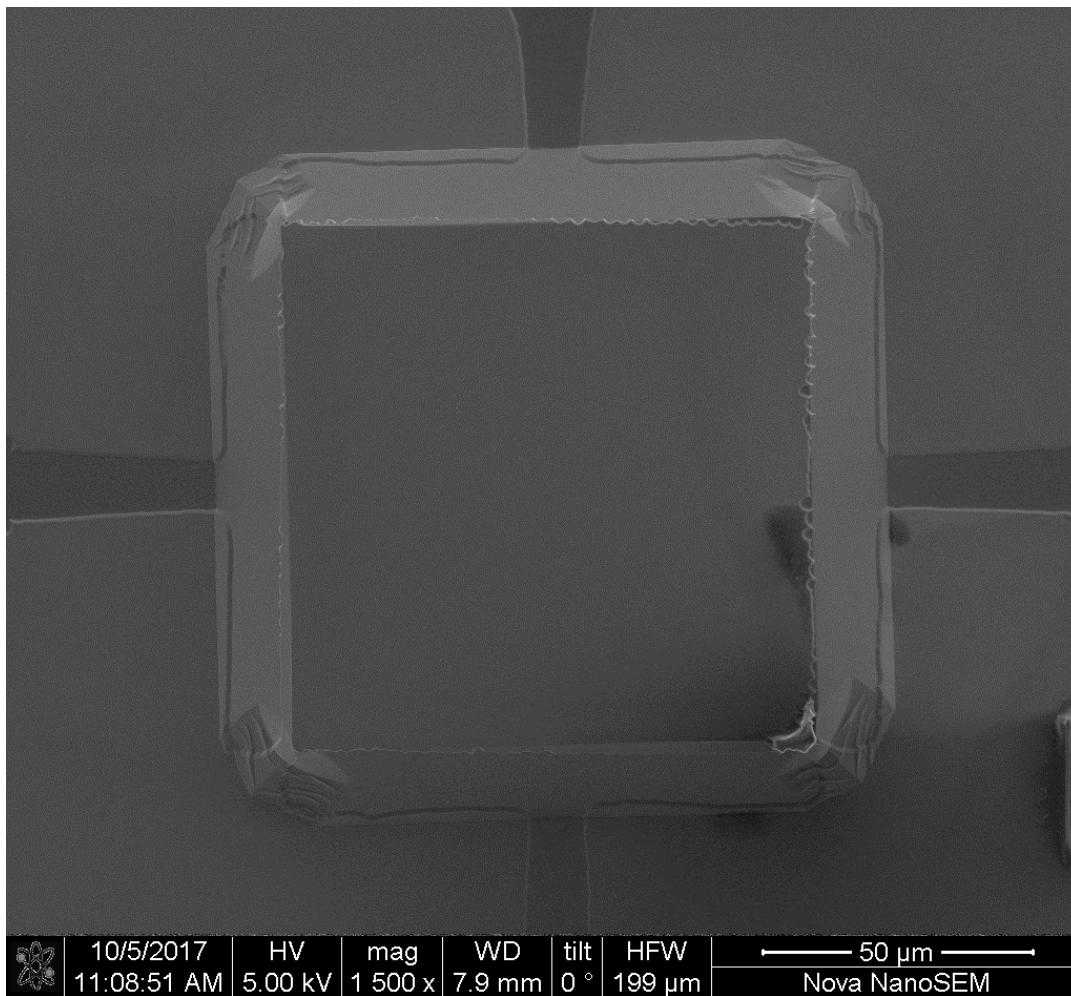


Figure 4-23 SEM image for raised pyramid

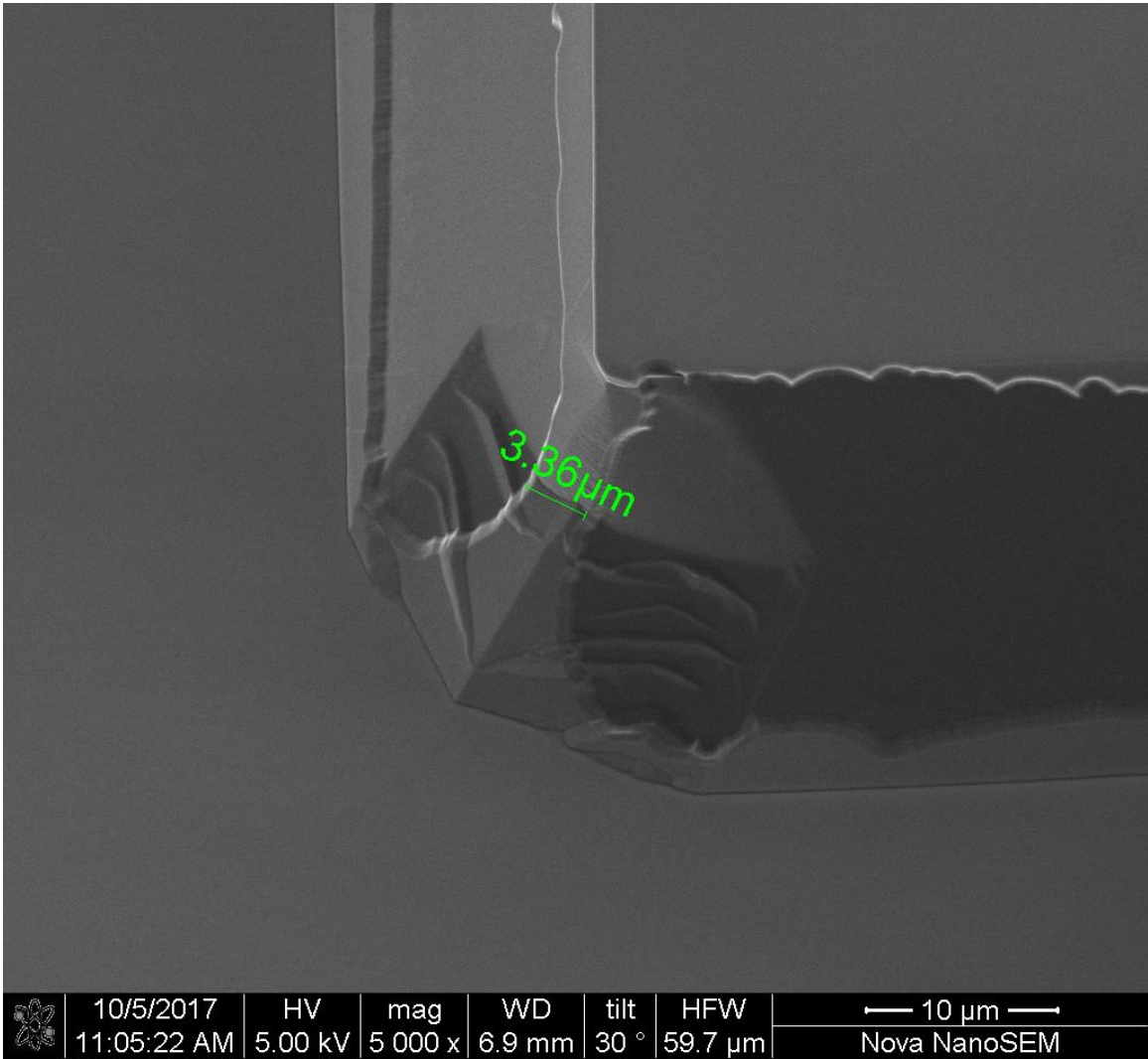


Figure 4-24 SEM image for raised pyramid at the corner

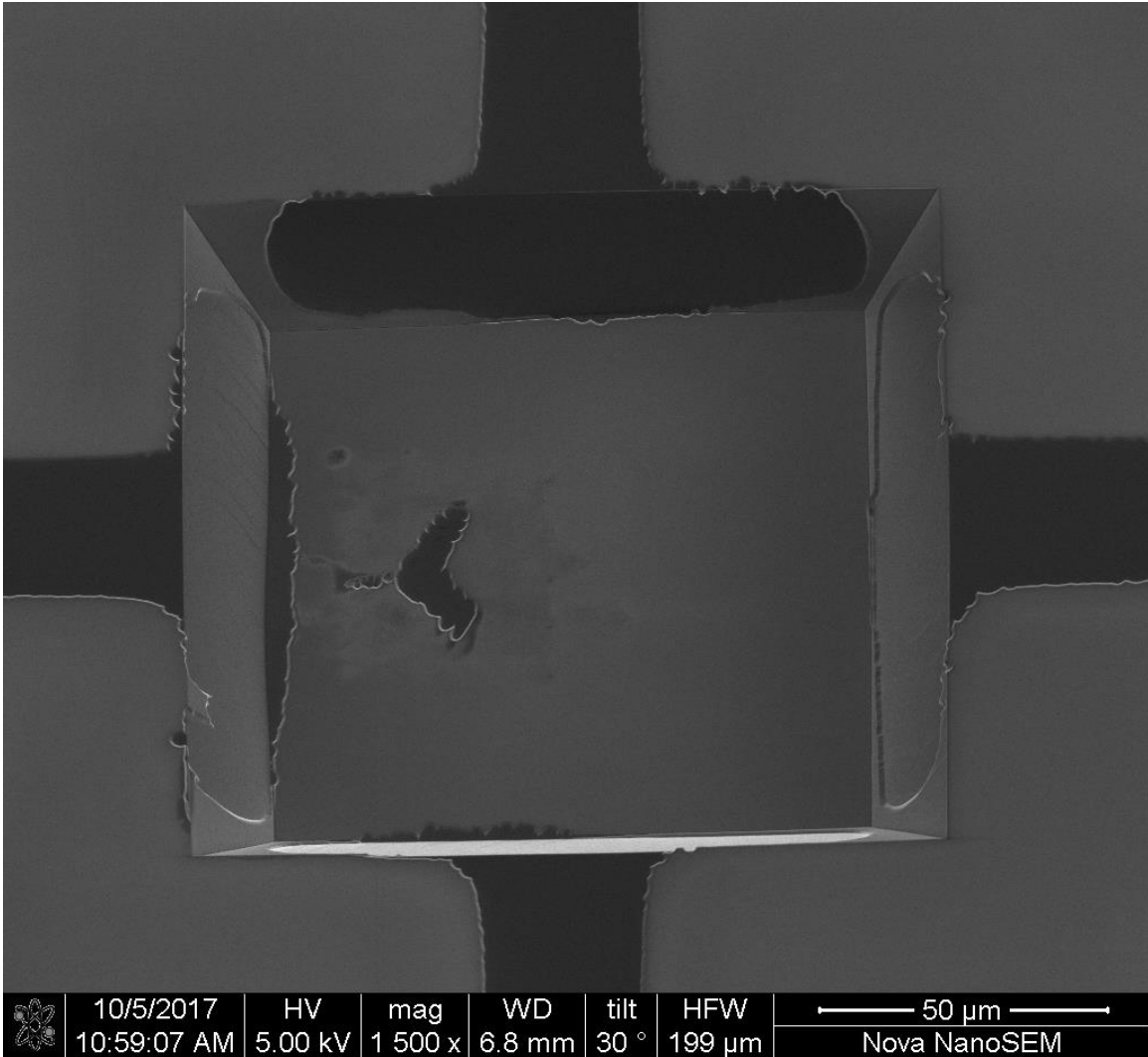


Figure 4-25 SEM image for inverted pyramid

Chapter 5. Results and Device Characterization

In this chapter, we are discussing the method and the result of testing and characterizing the fabricated device. The essential testing steps were done as follows: Characterization of the electrical properties of PN-junctions of a device, light sensitivity of the PN-junction, and angle estimation performance of the device in the 2D plane and 3D space. Since the fabrication process was manually achieved, none of a pair of photodiodes is identical. Therefore, the dark leakage current from each diode is different. Also, the sensitivity of the reverse bias current of each diode with different light is different as well. As a result, a calibration process before the device testing and performing were essential. Moreover, for actual industrial applications, the sensors will be exposed in daily life environment with numbers of light sources other than the target light source. The current generated by the photodiodes from the background light can be canceled by using a closed-loop amplifying circuit and with Arduino circuit board.

5.1. Diode characterization

This section analyzes the characteristic of the diodes from the fabricated devices including the IV curves for the forward bias region, reverse bias region and the sensitivity to the change of light intensity applying on the diode surface.

5.1.1. Forward bias region

All the diodes from the wire bonded devices were characterized by Keithley 2400 SMU. Positive supply was connected to the P-regions, and the negative one was connected to the N-regions of the diodes. The characteristics from the diodes on a four-pyramid chip were similar. Figure 5-1 indicates an IV response plot of one of the PN-junctions from a fabricated inverted pyramid by sweeping the voltage difference between P-region and N-region from 0V to 1V. In the forward bias region, the diode current started increasing at about 0.7V which was as expected since normal PN-junction formed on

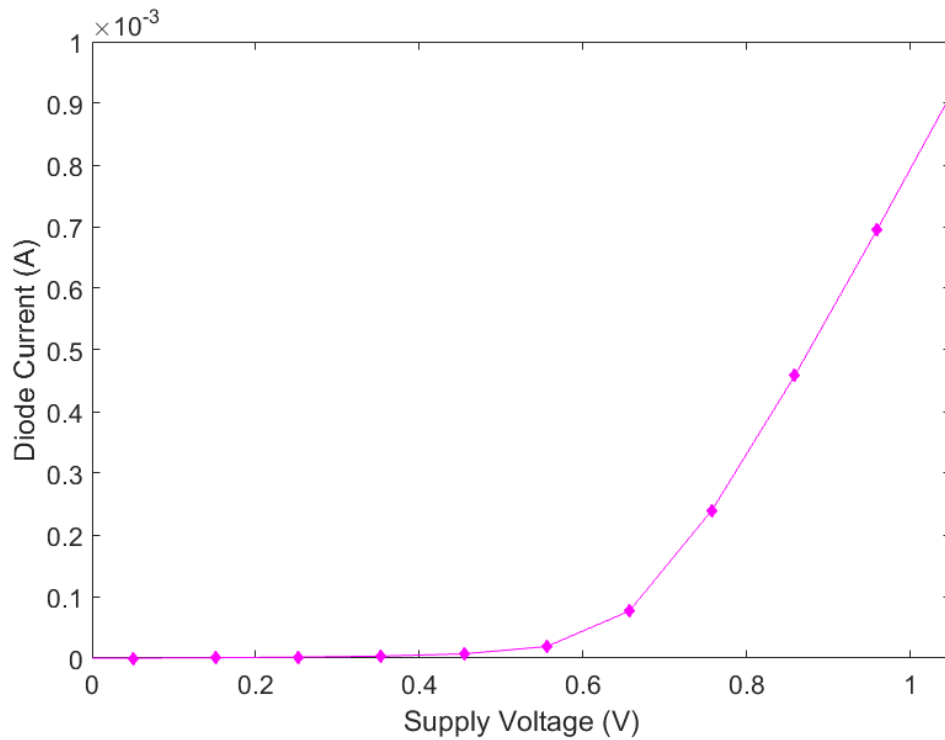


Figure 5-1 IV curve of a diode on the fabricated device with voltage sweeping from 0V to 1V

silicon has 0.7V turn-on voltage [59]. Moreover, when a diode is forward biased with a higher voltage, the series resistance of the diode will dominate in electrical contribution.

5.1.2. Reverse bias region

Similarly, a negative voltage was applied to the PN-junction from -10V to 0V. The result was shown in figure 5-2. The breakdown voltage for the diode was about -10.5V, that is, the diode can work with good performance within -10V supply voltage. Also, the reverse bias current of the diode was slowly and smoothly increasing from 0.15uA to 10uA with the supply voltage sweeping from 0V to -10V.

Therefore, in accuracy perspectives, the lower the voltage supplied to the diode, the less offset dark current was generated. The dark current would be negligible comparing to the current generated by the light photons if the diode was biased with 0V.

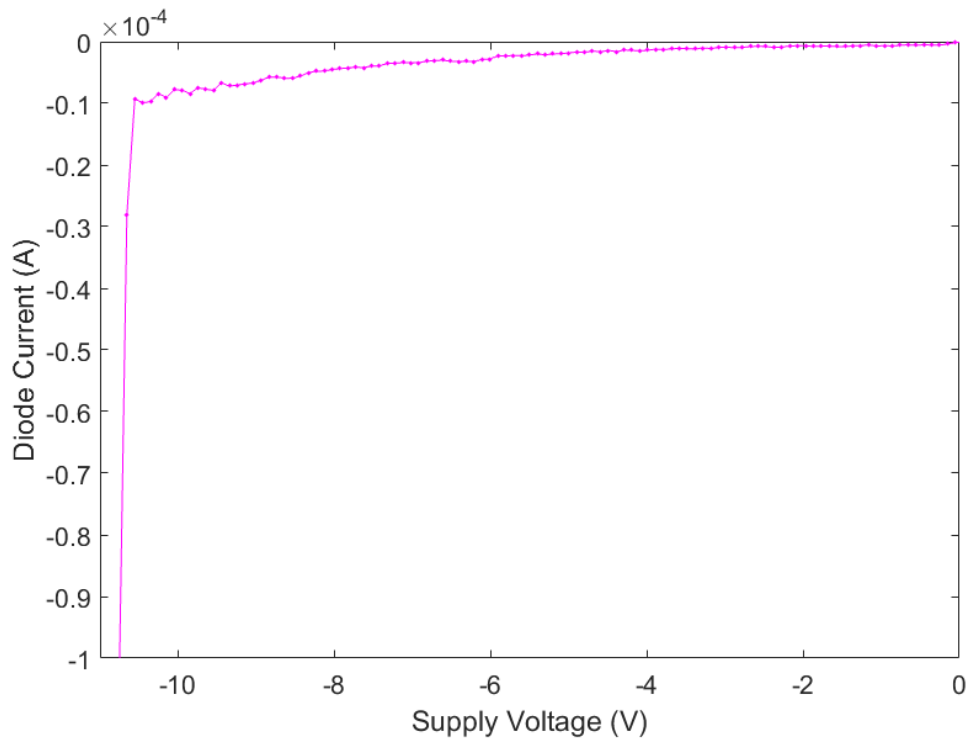


Figure 5-2 IV curve of a diode on the fabricated device with voltage sweeping from -11V to 0V

5.1.3. Sensitivity to light

Different light intensity was applied to the diode have been tested in the sections above. The actual irradiances of the light source were estimated by a commercial reference diode beside the fabricated device. The diode BPW34 was reverse biased with 5V and sitting under a light source with five different intensities. Five diode currents were collected respectively. By checking the datasheet [58], the corresponding irradiances from the light source to the diode surface were estimated. Under the same light intensities from the light source, diode currents generated by the diode from VLS were collected with 0V, 1V, 3V, and 5V reverse voltages. Figure 5-3 shows the plot of light irradiances vs. diode currents for the fabricated device with different reverse voltages. The plot shows that with higher reverse voltage, the rate of change in current was the highest, that is, the sensitivity was the greatest.

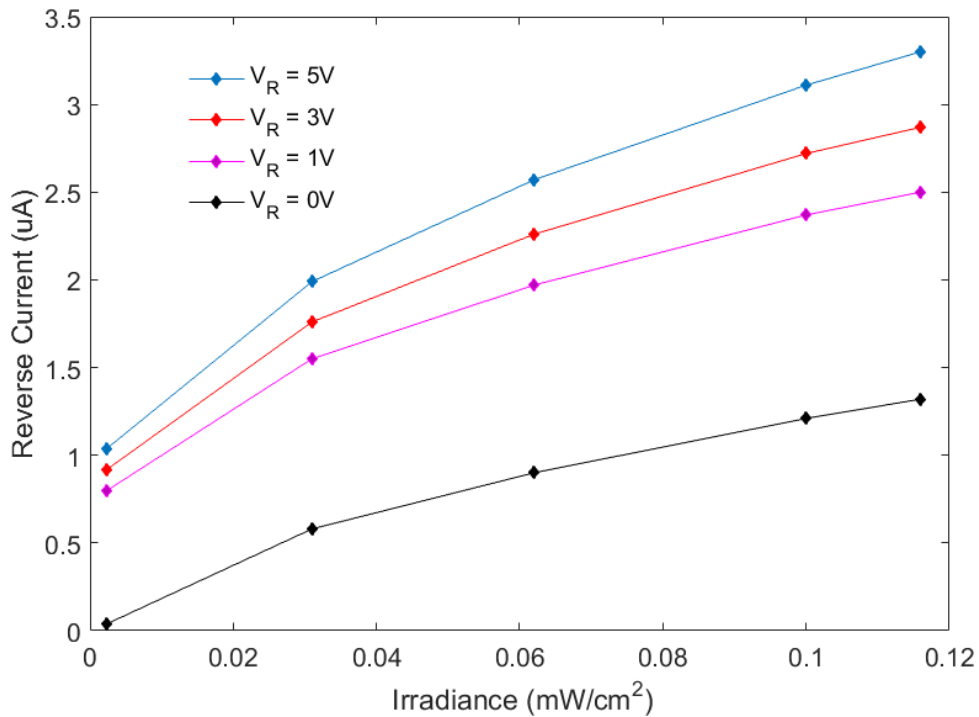


Figure 5-3 Irradiance vs. reverse diode current with different reverse voltages for a diode from VLS

When the diode was biased with a 5V reverse voltage, the sensitivity was calculated as $6.88 \mu A \cdot cm^2/mV$ comparing to $50 \mu A \cdot cm^2/mV$ for BPW34 commercial photodiode. It was reasonable to have such a different since the light sensing area of the VLS diode was much smaller than BPW34.

As a result, with certain amount of reverse voltage, the sensor has higher sensitivity but also higher dark current. To contribute a better performance and accuracy, building an amplifying circuit is essential for signal amplifying and dark/background current cancellation if the target light source has weak light intensity.

5.2. Test setup

5.2.1. Data processing

The equations developed from chapter 2 are assuming that all the sensors are identical without any dark currents. To make the sensors be able to proceed the algorithm with the equations, calibration is needed before the testing. Since each β value was only calculated by a pair of diodes with opposite directions on a single pyramid structure, the calibration was done pair by pair. At the beginning, the device was placed in dark environment with a ceramic lid covered on the package. Since a single calibration process was done with a pair of diodes, the dark currents from different directions could be named $I_{D_{left}}$ and $I_{D_{right}}$.

Once the dark currents from all the diodes were collected, the next step was to detect the relative sensitivities of the diodes. A light source was placed on top of a pyramid structure which $\beta=90^\circ$. The currents collected at this time were called $I_{1_{left}}$ and $I_{1_{right}}$. Another light source was applied again at the same spot with different light intensity. The currents will then change correspondingly as $I_{2_{left}}$ and $I_{2_{right}}$. With two different current values with two separate incident light intensities for one diode, the sensitivity of the diode could be determined. To make their sensitivities similar, a multiplier would be applied on either the left or the right diode:

$$M_{right} = \frac{I_{2_{left}} - I_{1_{left}}}{I_{2_{right}} - I_{1_{right}}} \quad (29)$$

If the raw data from left and right diodes are $I_{0_{left}}$ and $I_{0_{right}}$, then the processable data after calibration would be:

$$I_{left} = I_{0_{left}} - I_{D_{left}}, I_{right} = M_{right}(I_{0_{right}} - I_{D_{right}}) \quad (30)$$

Equation (30) was always applied with raw data before using the equations in device structure and operating principle chapter.

5.2.2. Testing interface

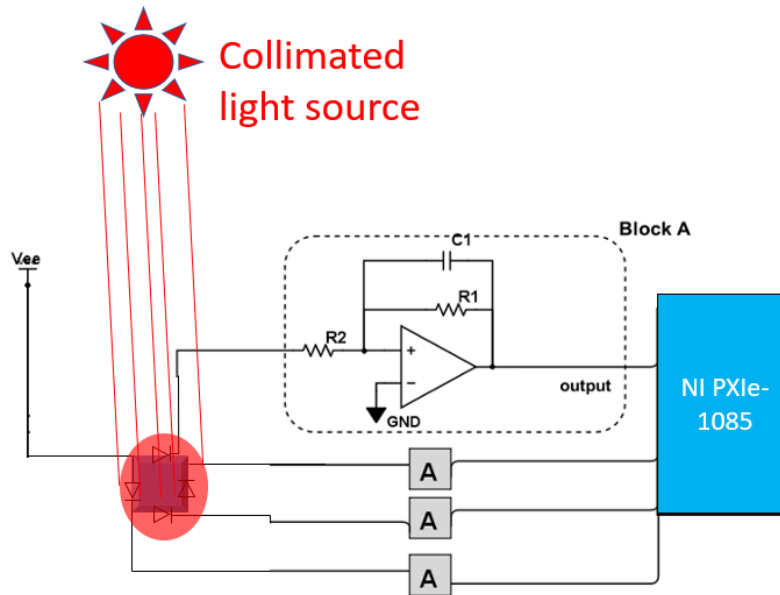


Figure 5-4 Device testing interface

The test setup for the fabricated devices is introduced in figure 5-4. The diodes on the pyramid facing four different directions were reverse biased. A shared P-junction connection for all four diodes was connected to V_{ee} , and each N-junction contact was connected to a transimpedance amplifier (converting current into voltage as shown in 'Block A'). The device was placed under collimated light beams from different directions. The outputs were collected by NI PXIe-1085 DMM. V_{ee} was $-1V$, R_1 was $1k\Omega$, and the op-amp was powered with $\pm 5V$. The estimated directions of the light beams were calculated in Matlab with the collected outputs.

The performance of the fabricated devices were tested inside a dark room with sidewalls covered by black blind paper. The room was about 7 ft. Height and 10 square ft. in the area. A collimated light source was mounted at the ceiling and pointing vertically to the center of the room. Also, an optical film was added in front of the light source so that a matrix pattern was generated from the light source as shown in Figure 5-5.

Even though the light intensity of each light source was not evenly distributed, the working sensor would still be able to estimate the angle and location of the beams. The reason for this was all the angle, distance and position estimations were based on the

ratio of the two opposite direction diodes instead of using the actual value of the current generated by the diodes. Therefore, the calculated result was regardless of the brightness of the light source itself. To test the efficiency and performance of the light sensor, the distance of each beam was measured as well as the height of the light source from the table the sensor was sitting. All the diodes from the pyramid were then powered and reverse biased. The sensor was placed and entirely covered by one of the beams, and all the outputs from all the diodes on the sensor were collected. After the data was collected, the sensor was moved to another beam, and the data collection was repeated. With the received data and the algorithm, the angles in 2D and the directions in 3D of the beams would be estimated.



Figure 5-5 Device testing environment and light source

5.3. Device functionality testing

The following sections are the comparisons between the actual values and the results calculated from the light sensing system. The sensor was placed at seven different locations under the light beams with corresponding angles in 2D and 3D. The locations the sensor was placed is indicated and numbered in table 5-1 and figure 5-6. The vertical distance between the light source and the testing bench was measured as $\approx 120\text{cm}$. The

distances between beams were measured so that the actual 2D and 3D angles of all the beams to the sensor were calculated as shown in table 5-1.

Table 5-1 Parameters for the beams for 2D angle estimation

Beam #	1	2	3	4	5	6	7
$\beta_{NS}(\circ)$	120	110	100	90	80	70	60
$\beta_{WE}(\circ)$	120	110	100	90	80	70	60

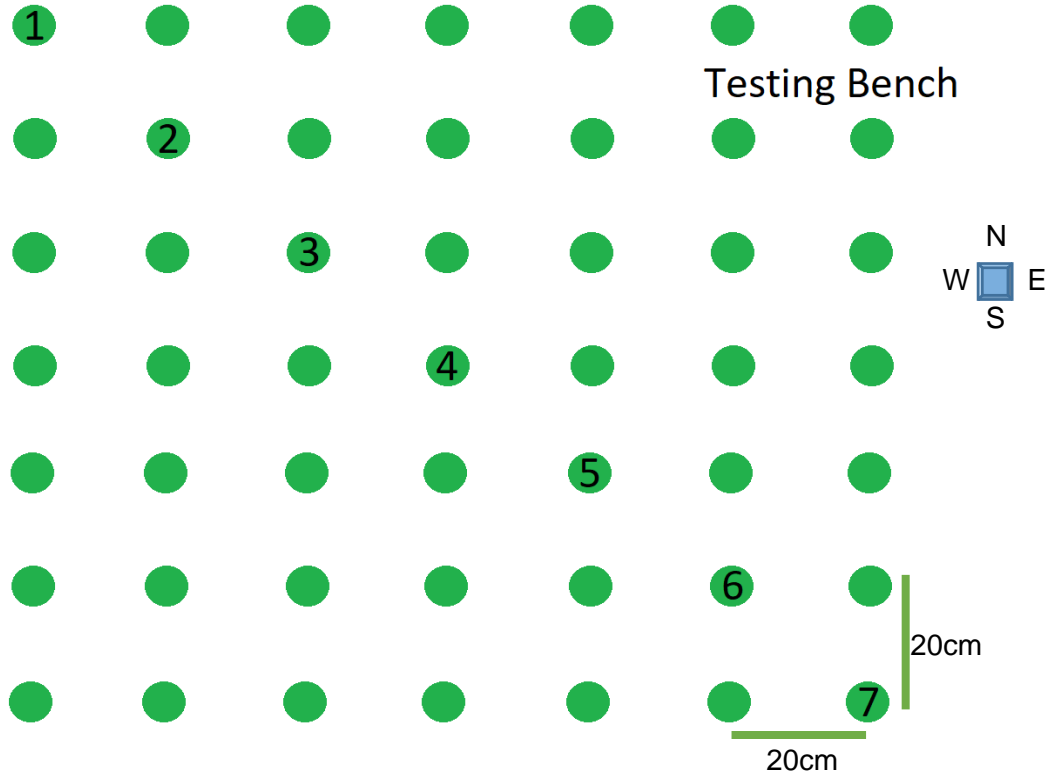


Figure 5-6 Light beams for testing the functionality of the VLS

where beam #4 was perpendicular to the work bench, that is, both β_{NS} and β_{WE} were 90° .

The outputs from four diodes were collected under all the light beams, then the measurements were repeated 10 times with the same device. The same measurement was also repeated once with another two devices.

Estimating the angle β

After data was collected from diodes, the angles were estimated by the equations developed in chapter 3. Figure 5-7 shows the comparison between estimated angles and actual angles for β_{NS} . As we could see from the figure, the determined result versus the actual result is showing a linear trend as desired. However, when the sensor was placed at either beam #1 or beam #7, the results were the furthest apart from the expected value. The mean value of the results from beam #1 was estimated at 65° which was 5° different from the real value, and the result from beam #7 has a 4° difference from the actual value.

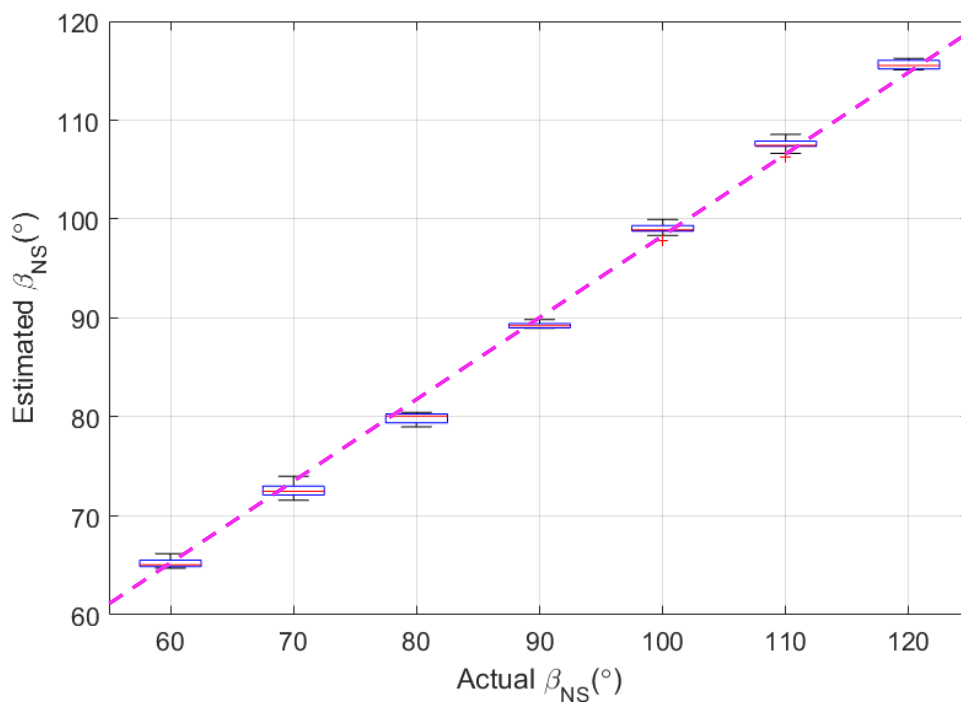


Figure 5-7 Comparison between estimated angles and actual angles for β_{NS} with one device and 10 repeated measurements

Moreover, with the data collected, β_{WE} were also estimated:

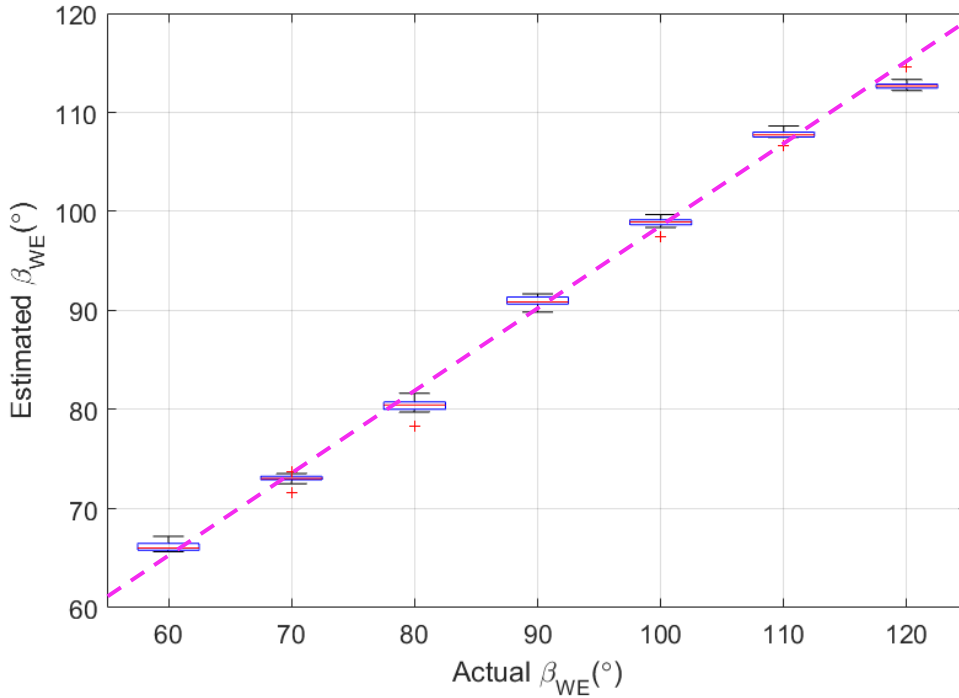


Figure 5-8 Comparison between estimated angles and actual angles for β_{WE} with one device and 10 repeated measurements

Similarly, the plot has a linear trend with the comparison between estimated angles and actual angles for β_{WE} . However, the estimated results from the West-East pair got more offset from the expected values. The mean value of the results from beam #1 was estimated at 67° which was 7° different from the real value, and the result from beam #7 has a 8° difference from the actual value. The performance across devices would be different based on the misalignment during the lithography process.

As shown from the figure 5-7 and figure 5-8, the further the device was placed from beam #4, the less accurate the result was. Since silicon dioxide is a reflective material [60], the results would be affected by the reflection to the silicon surface. Moreover, the result was also affected by the parasitic doped area for each diode (see figure 5-9). As indicated in the figure, the doped area on the <100> plane was about one-third of the one on the <111> plane.

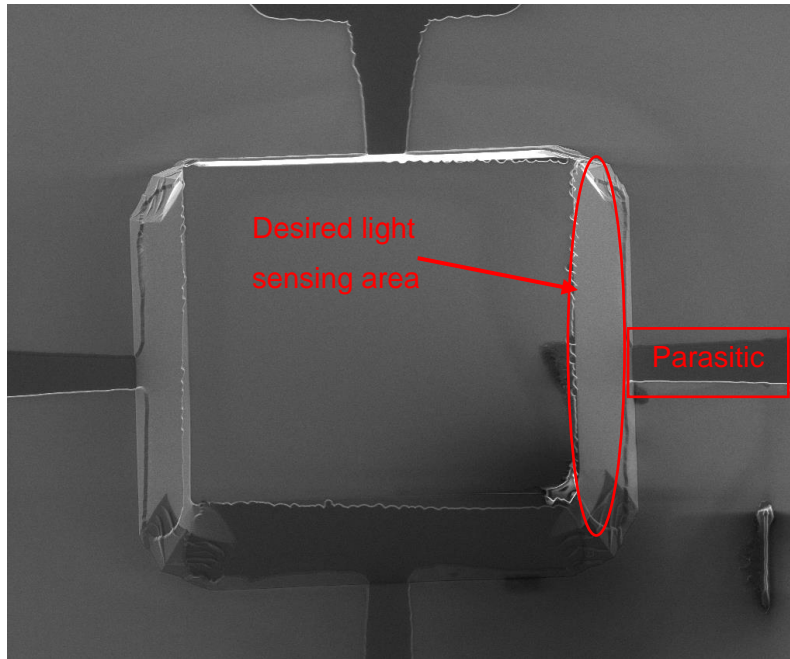


Figure 5-10 Comparison SEM image of a raised pyramid

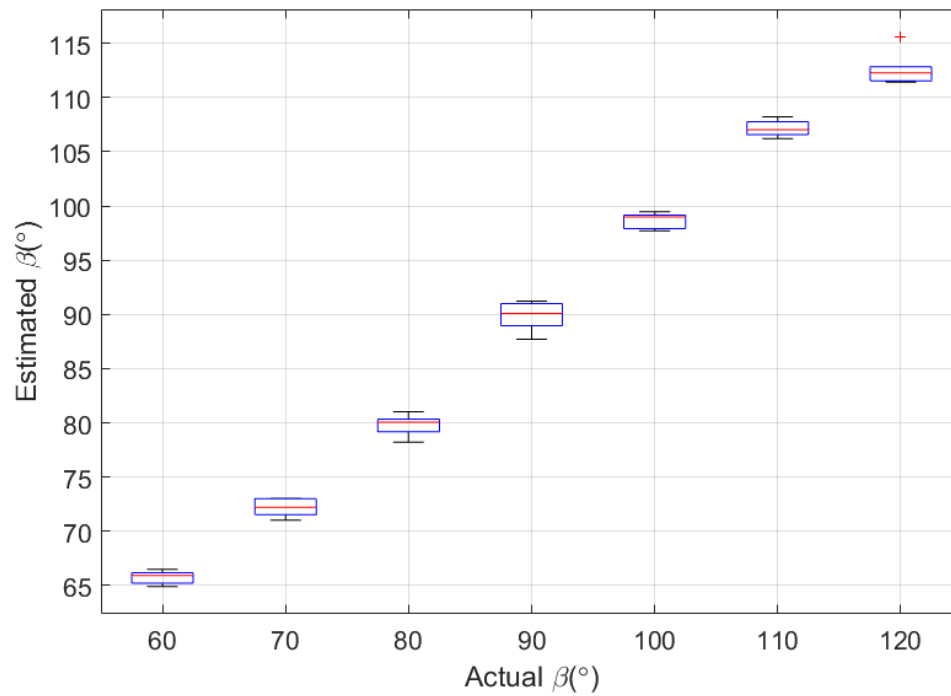


Figure 5-9 Comparison between estimated angles and actual angles for β with six pairs of optical detectors on pyramids

In order to test the repeatability among different devices, the measurements were

repeated with another two wire-bonded inverted pyramid packages. With one pyramid and the measurement with seven light beams, two β s could be estimated. Therefore, with three pyramids, six β would be estimated. Figure 5-10 demonstrates that, the testing results were repeatable with different devices. The highest deviation from the estimated results was 5° when β was at 90°.

Estimating the angle θ

With the estimated β_{NS} and β_{WE} results from figure 5-7 and figure 5-9, the corresponding 3D polar angle θ for each beam was also estimated.

Figure 5-11 indicates the comparison between the actual angles and the estimated angles for θ . Similarly, the further were the estimated polar angles from 0°, the less accurate were the results. The mean value of the results from beam #1 was estimated at

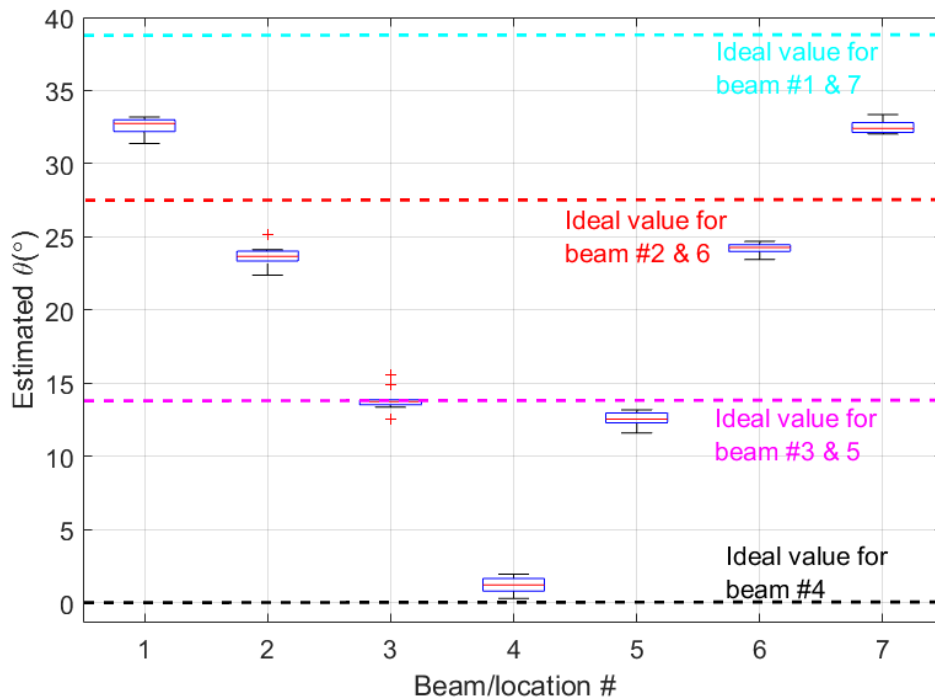


Figure 5-11 Comparison between estimated angles and actual angles for θ

32° which was 7° different from the real value, and the result from beam #7 has a 6° difference from the actual value. On the other hand, the mean value of the result at location #3 was at the ideal value which was 14°. As a result, the best range to perform the

functionality estimating the polar angles θ is within 10° . The range of vision could be increased by arranging the pyramids in arrays in the future.

Estimating the angle φ

Similarly, comparison between actual value and estimating value of φ was also completed as shown in figure 5-11.

The results from beam #1-3 were 42° , 44° and 43° respectively, which were close to the ideal value. Similarly, beam #5-7 also have the estimated values close to the actual values. Moreover, since the estimated value from beam #4 could be from -180° to 180° , the standard deviation of the result was much higher than the others.

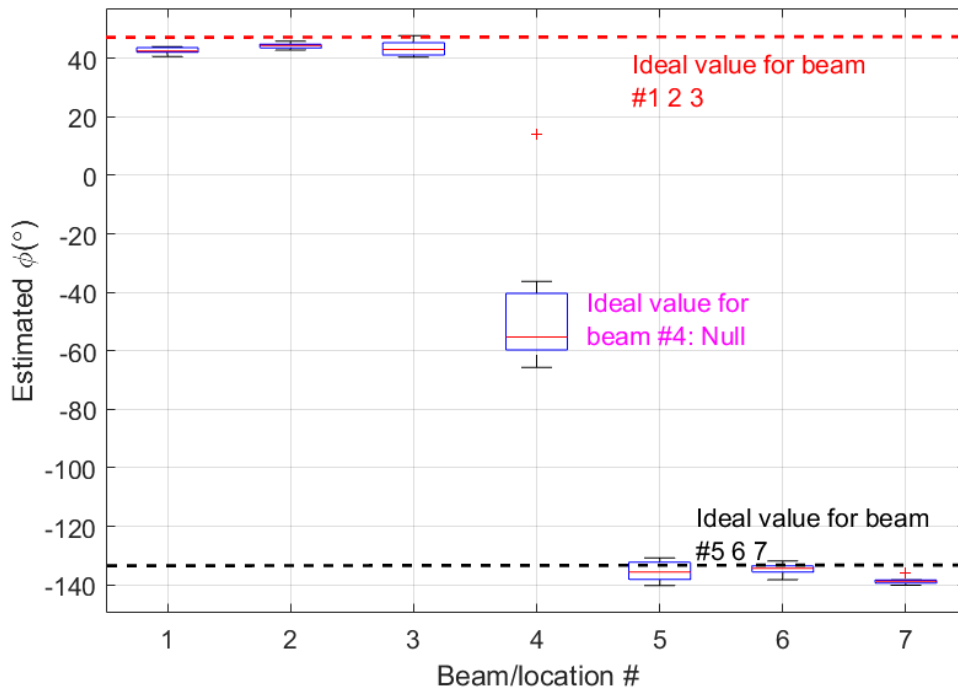


Figure 5-12 Comparison between estimated angles and actual angles for φ

In conclusion, the mathematical model of the VLS was proven by micro-scale fabricated raised/inverted pyramid structures. The functionality for estimating angles in 2D and in 3D was tested with multiple collimated light sources. The results from the measurements were repeatable with multiple measurements by one device, also with multiple devices.

Chapter 6. Conclusions and future work

In this thesis, a directional light sensor with the use of PN-junctions on both raised and inverted pyramid structures was investigated. The basic concept of the light detection was that the reversed bias current of a photodiode varies with the changing of light intensities applied on the surface of it. The direction of a targeted light source was detected by comparing all the reverse photo currents pass through photodiodes from different sidewalls of the pyramid structures.

The calculating algorithm was invented to detect the direction of a targeted light source related to the pyramid structure by a pyramid with four photodiodes on each side and the position of a light source in 3D space by two pyramids with a certain separation to each other. After that a signal processing method was created by a circuit with operating amplifiers in order to amplify the output current and cancel out the dark current. The electric circuit was integrated on a printed circuit board (PCB) which is designed as a shield of Arduino Due board with a plug for the package with the fabricated device. Afterwards, four masks for the actual light sensing devices were designed by CoventorWare. A fabrication process was done on a 4" silicon wafer with the designed masks. There were 6 different designs on the wafer: 20um, 60um and 100um in depth for both inverted and raised pyramid. Unfortunately, the designs for 60um and 100um were gave up base on the challenge of 3D lithography with spray coated photoresist for structures deeper than 20um. The wafer was diced by dicing saw into 7mm by 7mm small chips. Finally, the chips were wire bonded with gold wires into 40-pin packages.

The device was tested with light beams from high concentrated laser for the performance of directional detection. The performance was close to the simulation result, which with the largest variation as 7° . However, the estimation of position in 3D space cannot be tested with collimated light source since the beam size of the light is too small. Somehow the light sensor was not perfectly sensitive to normal light bulb because of the size and reflection from the surface. Fixing this issue will be the most essential future work.

To enhance the performance of the sensor for detecting normal size light source, we could:

- Increase the size of the pyramid structure in terms of depth and diameter. To increase the depth, a better method could be used for 3D lithography other than spray coating.
- Improve the design for the metal layer. Let the metal cover most of the area on the wafer to decrease the amount of reflection from the silicon surface.

Once the performance of the device is enhanced and it is able to detect the distance from light source to the device, more applications could be performed by the device. Another photodiode would be added on top of the raised pyramid or at the bottom of the inverted pyramid. An improved calculating algorithm with the new design could make the device be able to detect multiple light sources. Moreover, the pyramid structure with photodiodes could be fabricated into arrays. The new chip could be working with a camera together to estimate the actual size of the object in the image.

References

- [1] D. E. Whitney, C. A. Lozinski, and J. M. Rourke, "Industrial Robot Forward Calibration Method and Results," *J. Dyn. Sys., Meas., Control*, vol. 108, no. 1, pp. 1–8, Mar. 1986.
- [2] E. Abele, M. Weigold, and S. Rothenbücher, "Modeling and Identification of an Industrial Robot for Machining Applications," *CIRP Annals*, vol. 56, no. 1, pp. 387–390, Jan. 2007.
- [3] M. K. Roberts, M. A. Chikosky, and J. A. Speasl, "Electronic still video camera with direct personal computer (pc) compatible digital format output," US5138459A, 11-Aug-1992.
- [4] M. Ben-Ezra, A. Zomet, and S. K. Nayar, "Jitter camera: high resolution video from a low resolution detector," in *Proceedings of the 2004 IEEE Computer Society Conference on Computer Vision and Pattern Recognition, 2004. CVPR 2004.*, 2004, vol. 2, pp. II–II.
- [5] M. Ben-Ezra, A. Zomet, and S. K. Nayar, "Video super-resolution using controlled subpixel detector shifts," *IEEE Transactions on Pattern Analysis and Machine Intelligence*, vol. 27, no. 6, pp. 977–987, Jun. 2005.
- [6] S. Keen, J. Leach, G. Gibson, and M. J. Padgett, "Comparison of a high-speed camera and a quadrant detector for measuring displacements in optical tweezers," *J. Opt. A: Pure Appl. Opt.*, vol. 9, no. 8, p. S264, 2007.
- [7] A. Ramos, A. Ruíz, J. L. San Emeterio, and P. T. Sanz, "PSpice circuitual modelling of ultrasonic imaging transceivers including frequency-dependent acoustic losses and signal distortions in electronic stages," *Ultrasonics*, vol. 44, pp. e995–e1000, Dec. 2006.
- [8] G. Dong, Y. Hu, C. Jiang, L. Wang, and Y. Qiu, "Organic photocouplers consisting of organic light-emitting diodes and organic photoresistors," *Appl. Phys. Lett.*, vol. 88, no. 5, p. 051110, Jan. 2006.
- [9] L. R. Canfield, J. Kerner, and R. Korde, "Stability and quantum efficiency performance of silicon photodiode detectors in the far ultraviolet," *Appl. Opt., AO*, vol. 28, no. 18, pp. 3940–3943, Sep. 1989.
- [10] K. Kurosawa, K. Kuroki, and N. Saitoh, "CCD fingerprint method-identification of a video camera from videotaped images," in *Proceedings 1999 International Conference on Image Processing (Cat. 99CH36348)*, 1999, vol. 3, pp. 537–540 vol.3.

- [11] B. S. Wilburn, M. Smulski, H.-H. K. Lee, and M. A. Horowitz, "Light field video camera," in *Media Processors 2002*, 2001, vol. 4674, pp. 29–37.
- [12] E. S. Micko, "PIR motion sensor," US7399970B2, 15-Jul-2008.
- [13] J. Brugger, G. Beljakovic, M. Despont, N. F. de Rooij, and P. Vettiger, "Silicon micro/nanomechanical device fabrication based on focused ion beam surface modification and KOH etching," *Microelectronic Engineering*, vol. 35, no. 1, pp. 401–404, Feb. 1997.
- [14] H. Tanaka, S. Yamashita, Y. Abe, M. Shikida, and K. Sato, "Fast etching of silicon with a smooth surface in high temperature ranges near the boiling point of KOH solution," *Sensors and Actuators A: Physical*, vol. 114, no. 2, pp. 516–520, Sep. 2004.
- [15] S. P. Garcia, H. Bao, and M. A. Hines, "Etchant Anisotropy Controls the Step Bunching Instability in KOH Etching of Silicon," *Phys. Rev. Lett.*, vol. 93, no. 16, p. 166102, Oct. 2004.
- [16] R. A. Millikan, "Einstein's Photoelectric Equation and Contact Electromotive Force," *Phys. Rev.*, vol. 7, no. 1, pp. 18–32, Jan. 1916.
- [17] L.-Y. Ku and S.-C. Liao, "Solar street light," US20140355259A1, 04-Dec-2014.
- [18] L.-C. Lai, "Night lamp," US7419294B2, 02-Sep-2008.
- [19] P. S. Serebrennikov and V. A. Kholodnov, "Character of photocurrent dependence on two-level recombination impurity concentration in an intrinsic photoconductive detector," in *International Conference on Photoelectronics and Night Vision Devices*, 1999, vol. 3819, pp. 122–127.
- [20] B. Polyakov *et al.*, "High-Density Arrays of Germanium Nanowire Photoresistors," *Advanced Materials*, vol. 18, no. 14, pp. 1812–1816, Jul. 2006.
- [21] S. E. Plunkett, S. Propst, and M. S. Braiman, "Supported planar germanium waveguides for infrared evanescent-wave sensing," *Appl. Opt., AO*, vol. 36, no. 18, pp. 4055–4061, Jun. 1997.
- [22] R. Soref, "Mid-infrared photonics in silicon and germanium," *Nature Photonics*, vol. 4, pp. 495–497, Aug. 2010.
- [23] M. C. Clerc and P. E. Carroll, "Automatic gain control employing photoresistors," US3379991A, 23-Apr-1968.

- [24] Silonex Inc., "Photoconductive Cells," TO-18 Photocells.
- [25] D. E. Groom, "Silicon photodiode detection of bismuth germanate scintillation light," *Nuclear Instruments and Methods in Physics Research*, vol. 219, no. 1, pp. 141–148, Jan. 1984.
- [26] J. Geist, "Silicon photodiode front region collection efficiency models," *Journal of Applied Physics*, vol. 51, no. 7, pp. 3993–3995, Jul. 1980.
- [27] G. F. Amelio, M. F. Tompsett, and G. E. Smith, "Experimental Verification of the Charge Coupled Device Concept," *Bell System Technical Journal*, vol. 49, no. 4, pp. 593–600, Apr. 1970.
- [28] C. D. Mackay, "Charge-Coupled Devices in Astronomy," *Annual Review of Astronomy and Astrophysics*, vol. 24, no. 1, pp. 255–283, 1986.
- [29] Z. Zivkovic and C. C. Tak, "Integrated sensor chip package with directional light sensor, apparatus including such a package and method of manufacturing such an integrated sensor chip package," US9666637B2, 30-May-2017.
- [30] I. Todhunter, *Spherical Trigonometry, for the Use of Colleges and Schools: With Numerous Examples*. Macmillan, 1863.
- [31] A. W. Snyder and J. Love, *Optical Waveguide Theory*. Springer Science & Business Media, 2012.
- [32] "Historical Background and Development of Soviet Quasioptics at Near-mm and Sub-mm Wavelengths," in *History of Wireless*, John Wiley & Sons, Ltd, 2006, pp. 473–542.
- [33] D. Gacemi, J. Mangeney, R. Colombelli, and A. Degiron, "Subwavelength metallic waveguides as a tool for extreme confinement of THz surface waves," *Scientific Reports*, vol. 3, p. 1369, Mar. 2013.
- [34] D. a. Pinnow, T. c. Rich, F. w. Ostermayer, and M. DiDomenico, "Fundamental optical attenuation limits in the liquid and glassy state with application to fiber optical waveguide materials," *Appl. Phys. Lett.*, vol. 22, no. 10, pp. 527–529, May 1973.
- [35] C. C. Liebe, S. Mobasser, Y. Bae, C. J. Wrigley, J. R. Schroeder, and A. M. Howard, "Micro Sun sensor," in *Proceedings, IEEE Aerospace Conference*, 2002, vol. 5, pp. 5–5.

- [36] A. Trebi-Ollenu, T. Huntsberger, Y. Cheng, E. T. Baumgartner, B. Kennedy, and P. Schenker, "Design and analysis of a sun sensor for planetary rover absolute heading detection," *IEEE Transactions on Robotics and Automation*, vol. 17, no. 6, pp. 939–947, Dec. 2001.
- [37] C. C. Liebe and S. Mobasser, "MEMS based Sun sensor," in *2001 IEEE Aerospace Conference Proceedings (Cat. No.01TH8542)*, 2001, vol. 3, pp. 3/1565-3/1572 vol.3.
- [38] Z. Dong Hao, "Vector Light Sensor," Co-op Technical Report, Dec. 2016.
- [39] T. Cevik and S. Yilmaz, "An overview of visible light communication systems," *CoRR*, vol. abs/1512.03568, 2015.
- [40] I. El-chami, S. Vosoogh-Grayli, D. Zhuo, and B. Bahreyni, "A vector light detector for proximity sensing applications," *2016 IEEE SENSORS*, pp. 1–3, 2016.
- [41] G. K. Mayer, H. L. Offereins, H. Sandmaier, and K. Kühl, "Fabrication of Non-Underetched Convex Corners in Anisotropic Etching of (100)-Silicon in Aqueous KOH with Respect to Novel Micromechanic Elements," *J. Electrochem. Soc.*, vol. 137, no. 12, pp. 3947–3951, Jan. 1990.
- [42] B. Fischl, M. I. Sereno, and A. M. Dale, "Cortical Surface-Based Analysis: II: Inflation, Flattening, and a Surface-Based Coordinate System," *NeuroImage*, vol. 9, no. 2, pp. 195–207, Feb. 1999.
- [43] S. Banerjee, "Revisiting Spherical Trigonometry with Orthogonal Projectors," *The College Mathematics Journal*, vol. 35, no. 5, pp. 375–381, Nov. 2004.
- [44] M. Steiner, "Mathematical explanation," *Philosophical Studies*, vol. 34, no. 2, pp. 135–151, Aug. 1978.
- [45] B. E. Deal and A. S. Grove, "General Relationship for the Thermal Oxidation of Silicon," *Journal of Applied Physics*, vol. 36, no. 12, pp. 3770–3778, Dec. 1965.
- [46] S. Roddaro, P. Pingue, V. Piazza, V. Pellegrini, and F. Beltram, "The Optical Visibility of Graphene: Interference Colors of Ultrathin Graphite on SiO₂," *Nano Lett.*, vol. 7, no. 9, pp. 2707–2710, Sep. 2007.
- [47] E. Kontturi, P. C. Thüne, and J. W. Niemantsverdriet, "Novel method for preparing cellulose model surfaces by spin coating," *Polymer*, vol. 44, no. 13, pp. 3621–3625, Jun. 2003.

- [48] M. Rezaei, "Rapid Production of Nano-pixel-based Color Imageries," Master Thesis, Simon Fraser University, British Columbia, Canada, 2015.
- [49] A. Merlos, M. Acero, M. H. Bao, J. Bausells, and J. Esteve, "TMAH/IPA anisotropic etching characteristics," *Sensors and Actuators A: Physical*, vol. 37–38, pp. 737–743, Jun. 1993.
- [50] T. W. Sigmon, W. K. Chu, E. Lugujo, and J. W. Mayer, "Stoichiometry of thin silicon oxide layers on silicon," *Appl. Phys. Lett.*, vol. 24, no. 3, pp. 105–107, Feb. 1974.
- [51] S. Guha, M. D. Pace, D. N. Dunn, and I. L. Singer, "Visible light emission from Si nanocrystals grown by ion implantation and subsequent annealing," *Appl. Phys. Lett.*, vol. 70, no. 10, pp. 1207–1209, Mar. 1997.
- [52] Q. Zhang, L. Liu, and Z. Li, "A new approach to convex corner compensation for anisotropic etching of (100) Si in KOH," *Sensors and Actuators A: Physical*, vol. 56, no. 3, pp. 251–254, Sep. 1996.
- [53] W. Fan and D. Zhang, "A simple approach to convex corner compensation in anisotropic KOH etching on a (1 0 0) silicon wafer," *J. Micromech. Microeng.*, vol. 16, no. 10, p. 1951, 2006.
- [54] K. E. Bean and K. E. Bean, "Anisotropic etching of silicon," *IEEE Transactions on Electron Devices*, vol. 25, no. 10, pp. 1185–1193, Oct. 1978.
- [55] P. Pal, K. Sato, and S. Chandra, "Fabrication techniques of convex corners in a (1 0 0)-silicon wafer using bulk micromachining: a review," *J. Micromech. Microeng.*, vol. 17, no. 10, p. R111, 2007.
- [57] A. del Campo and C. Greiner, "SU-8: a photoresist for high-aspect-ratio and 3D submicron lithography," *J. Micromech. Microeng.*, vol. 17, no. 6, p. R81, 2007.
- [58] A. Rasouli, "Employing Piezjunction Effect for Resonant Micro-Device Applications," PhD Dissertation, Simon Fraser University, British Columbia, Canada, 2016.
- [59] Vishay Semiconductors, "Silicon PIN Photodiode," BPW34 Datasheet, 2011.
- [60] M. Cid, N. Stem, C. Brunetti, A. F. Beloto, and C. A. S. Ramos, "Improvements in anti-reflection coatings for high-efficiency silicon solar cells," *Surface and Coatings Technology*, vol. 106, no. 2, pp. 117–120, Aug. 1998.

Appendix A. Fabrication details

Details of silicon anisotropic etching process

Etchant	Solution preparation	Etch rate	Etched depth
KOH	<ul style="list-style-type: none">-Place 500ml of 45% KOH solution into baker, then add 365ml of DI water.-Heat up to 80°C, then add 150ml IPA. Place wafer into the solution when the temperature was stable at 80°C.-Turn on magnetic spinner at 120RPM-Keep wafer in solution for 20 minutes	0.158Å/s	19µm
TMAH	<ul style="list-style-type: none">-Place 1L of TMAH solution, heat up to 80°C, then add 200ml IPA. Place wafer into the solution when the temperature was stable at 90°C.-Turn on magnetic spinner at 120RPM-Keep wafer in solution for 3 minutes	0.056Å/s	1µm

Details of the fabrication process

Run sheet	Recipe
1. RCA – 1	80°C for 10 minutes
2. HF Dip	Room temperature for 30 seconds
3. RCA – 2	80°C for 10 minutes
4. Wet oxidation	1100°C for 55 minutes Dry N2 @ 4 scfh
5. Hot plate	110°C for 2 minutes Cool down for 1 minute
6. HMDS deposition	5 minutes
7. Spin coating	@ 300RPM for 60s
8. Hot plate	90°C for 1 minutes Cool down for 1 minute
9. Exposure	4 seconds
10. Hot plate	110°C for 1 minute Cool down for 1 minute
11. Development	120 seconds

12. Water rinse	3 minutes
13. Hot plate	110°C for 3 minutes
14. BOE etching	9 minutes 30 seconds
15. Strip PR	<ul style="list-style-type: none"> - Acetone 4 mins in sonicator - IPA 2 mins - Water 2 mins
16. KOH etching	80°C for 20 minutes
17. TMAH etching	90°C for 3 minutes
18. Oxide etching	9 minutes 30 seconds
19. RCA clean	<ul style="list-style-type: none"> -80°C for 10 minutes -Room temperature for 30 seconds -80°C for 10 minutes
20. Wet oxidation	1100°C for 55 minutes Dry N2 @ 4 scfh
21. Hot plate	110°C for 2 minutes Cool down for 1 minute
22. HMDS deposition	5 minutes

23. Spray coating	6 layers diluted 1:1 AZ 703 PR
24. Hot plate	90°C for 3 minutes
25. Exposure	30 seconds
26. Hot plate	110°C for 3 minutes
27. Development	3 minutes
28. Hot plate	110°C for 3 minutes
29. BOE etching	12 minutes 45 seconds
30. Strip PR	Acetone 4 mins in sonicator IPA 2 mins Water 2 mins
31. RCA – 1 & RCA – 2	-80°C for 10 minutes -80°C for 10 minutes
32. Ion implantation	Dose: 1.2E12, Energy: 20keV Dose: 4E14, Energy: 10keV
33. BOE etching	12 minutes 45 seconds
34. RCA clean	-80°C for 10 minutes -Room temperature for 30 seconds -80°C for 10 minutes

35. Wet oxidation	900°C for 2 hours Dry N2 @ 4 scfh
36. Hot plate	110°C for 2 minutes Cool down for 1 minute
37. HMDS deposition	5 minutes
38. Spray coating	6 layers diluted 1:1 AZ 703 PR
39. Hot plate	90°C for 3 minutes
40. Exposure	30 seconds
41. Hot plate	110°C for 3 minutes
42. Development	3 minutes 30 seconds
43. Hot plate	110°C for 3 minutes
44. BOE etching	10 minutes
45. Strip PR	Acetone 4 mins in sonicator IPA 2 mins Water 2 mins
46. Hot plate	110°C for 2 minutes Cool down for 1 minute
47. HMDS deposition	5 minutes

48. Spray coating	6 layers diluted 1:1 AZ 703 PR
49. Hot plate	90°C for 3 minutes
50. Exposure	30 seconds
51. Hot plate	110°C for 3 minutes
52. Development	3 minutes 30 seconds
53. Hot plate	110°C for 3 minutes
54. RCA – 1 & RCA – 2	-80°C for 10 minutes -80°C for 10 minutes
55. HF Dip	Right before metal deposition -Room temperature for 30 seconds
56. Evaporation Al/Si deposition	16cm Al/Si wire Current at 35A Deposition rate ~ 0.5nm/s
57. Lift-off	Soak in Acetone for 10 minutes Sonication for 10 minutes Rinse with IPA for 1 minute Water rinse for 3 minutes

Appendix B. Feasible parameters for wire bonding



Always keep the same parameter for Al/Si pad to gold package with gold wires

Base Height	10cm
Loop	6.8
Tail	7.5
1st Power	2.5
2nd Power	4.4
1st Time	4.8
2nd Time	5.6
1st Force	1
2nd Force	1.2